Scuola Normale Superiore

Ph. D. Thesis

Low lying excitations of few electrons in quantum dots

César Pascual García

Advisors

Dr. Vittorio Pellegrini
Prof. Aron Pinczuk

2007

A discussion with many faces is difficult to follow. Similarly, the physics of the interactions among electrons can be better understood when the number of particles is reduced, and yet the conversation can be even more interesting. The drawings shown on the cover and at the introduction of each chapter are by *Vicente García García*, and inspired by this fact.

To my parents and brother

To aunts Fernanda and Maru

To Milagros Barrio for her great life example

Contents

Introduction

Studies of quantum states that result from strongly interacting fermionic quasi-particles under conditions of greatly reduced dimensions are among the topics at the current frontiers of fundamental and applied physics. Semiconductor quantum dots (QDs) are artificial structures in which electrons are confined by a potential that can be controlled at will into dimensions of length comparable to the de-Broglie wavelength [1]. In the low-density few-electron regime QDs should exhibit new emergent states of quasi-particles, not observable in any other systems [2, 3, 4, 5, 6]. Requests for experiments able to probe electronic interactions in QDs have also been triggered by possible applications in the area of quantum computation [7, 8] and in particular by the proposals of solid state quantum bits [9, 10, 11, 12]. The measurement of interaction effects in QDs is a very challenging task since often the experiments are not sensible enough or correlations are perturbed by the techniques used [13, 14, 15]. Inelastic scattering of particles has revealed as a very powerful method to probe interaction effects in other systems. For example, scattering of neutrons by nucleons led to the discovering of the fine structure of atomic nuclei [16], or in the solid state field, inelastic scattering of photons by two dimensional electron gases is often used

to study many body interactions of quasi-particles confined in semiconductor hetero-structures [17, 18]. Inelastic light scattering experiments that study electronic states in semiconductors [19] offer numerous advantages, i.e. they are sensible to charge and spin neutral excitations. However these experiments are very demanding and there are very few groups that have reported inelastic light scattering measurements by electrons confined in QDs. In GaAs-based QDs, these works are restricted to systems where the number of quasi-particles is very high [20, 21, 22].

This thesis focuses on neutral excitations of few-electrons states in nano-fabricated QDs measured by inelastic light scattering. The analysis of the spectra demonstrate that this technique can open a venue in the study of quasi-particles at the nanoscale.

A model of electronic states confined in QDs is presented in the first chapter, while the second one provides a survey of the relevant experimental studies in this field. Special attention is paid to the process of inelastic light scattering by introducing a description of the selection rules for the scattering processes by electrons in semiconductor QDs. Chapter 3 describes the nano-fabrication techniques of doped AlGaAs/GaAs QDs and the different setups used for the measurements. Experiments performed with μ-photoluminescence that demonstrate the confinement and the homogeneity of the fabricated QDs are reported at the end of this chapter.

Chapter 4 reports inelastic light scattering spectra from QDs with many electrons. In these experiments the atomic-like shell structure of the electronic states is demonstrated. The framework used to describe this regime of highly populated QDs is similar to the one used for transport experiments in the Coulomb blockade regime. Observations of tunneling excitations in coupled quantum dots with inelastic light scattering will also be presented.

The most innovative results of this work are presented in chapter 5 that focuses on the study of interaction phenomena that take place in QDs in the few electron regime. The correlations that occur among the electrons deeply affect the inelastic light spectra in these systems. The main outcome regards the case of QDs with four electrons where strong correlation effects have been found in the behavior of spin and charge collective excitations. Light scattering spectra from these dots at zero and finite perpendicular magnetic fields will be presented. The evaluation of the excitation spectra as a function of the magnetic field reveals a ground-state transition between correlated states of the four electrons with different spin configurations.

Chapter

1

Electronic states in semiconductor quantum dots

Electrons confined in semiconductor nano-structures to a region comparable to their De Broglie wavelength display a behavior dictated by quantum mechanics. The QD is an example of a quantum confined region. QDs are usually referred as artificial atoms since their electronic properties are similar to those of electrons in atomic orbitals. The electronic industry has stimulated great developments in the fabrication techniques of semiconductor devices and it is currently possible to tailor at will the properties of semiconductor QDs.

The description of electrons in QDs involves the interaction of a very large number of particles, accounting for the nuclei of atoms forming the crystal, and the electrons. In a crystal most of the electrons are trapped by the potential of the nuclei, and only a few electrons are free to move in a potential field created by the ions. In a semiconductor QD, electrons are also subjected to a confining potential caused by an applied electrical field or by a change in the chemical potential due to a discontinuity in the distribution of atoms.

This chapter presents a model capable of describing the basic physics of the electronic states in QDs.

1.1 Single particle states

The Born-Oppenheimer approximation that decouples the motion of the ions from the electrons is adopted in the following. The effects of nuclear vibrations can be taken as a perturbation leading to an electron-phonon interaction but they shall be neglected here. Within these approximations the QD electronic Hamiltonian is given by:

$$H = \sum_{i}^{N_e} H_0(\mathbf{r}_i) + \frac{1}{2}\sum_{i\neq j}\frac{e^2}{|\mathbf{r}_i - \mathbf{r}_j|} \ , \tag{1.1}$$

where $\mathbf{r_i}$ is the space coordinate of the i^{th} electron, N_e is the total number of free electrons, e is the electron charge, and:

$$H_0(\mathbf{r_i}) = \frac{\mathbf{p_i}^2}{2m_e} + V_{ions}(\mathbf{r_i}) \tag{1.2}$$

constitutes the single particle Hamiltonian of electrons, with $\mathbf{p_i}$ the momentum of the electron, m_e the electron mass, and V_{ions} the potential created by the ions. The potential of core electrons in the atoms is included in $V_{ions}(\mathbf{r})$. The second term in the right side of Eq. 1.1 represents the Coulomb interactions among the electrons that are not bound to the ion cores (free electrons).

In the following the solutions of $H_0(\mathbf{r})$ will be derived and then the interaction term will be treated as a perturbation. In the single particle approximation the electrons occupy the lowest energy states dictated by Eq. 1.2. In the presence of electron-electron interactions the single particle picture is still the starting point to build a set of wave-functions that constitutes a complete orthonormal base from which one can create models for the many-body physics.

1.1.1 Envelope Function and effective mass approximation

The characteristic dimensions of the semiconductor QDs described here are at least one or two orders of magnitude larger than the semiconductor lattice constant. Thus, the total potential V_{ions} can be separated into a fast oscillating part (V_{crys}) having the crystal periodicity and another one (V_{dot}) that varies on the length scale of the QD.

In the absence of band degeneracy, the wave-function of an electron subjected to this kind of potential can be described by a fast oscillating part modulated by an envelope wave-function:

$$\Psi_l(\mathbf{r}) = \psi(\mathbf{r}) u_l(\mathbf{r}, \mathbf{k}) \tag{1.3}$$

where $u_l(\mathbf{r}, \mathbf{k})$ is the rapidly oscillating Bloch function and $\psi(\mathbf{r})$ is the envelope function defined by the confining potential responsible of the QD formation and l is the band index.

The case of the valence band is more complex owing to the mixing of heavy, and light holes and the influence of spin-orbit interactions [23]. Hole states play an important role in the resonant inelastic light scattering spectra [24] as it will be discussed in section 2.3.

1.1.2 The single particle Hamiltonian for cylindrical quantum dots

The single particle Hamiltonian for electrons in the QD conduction band within the effective mass and envelope function approximation reads:

$$H_{space} = \frac{1}{2m^*}\left[\mathbf{p} - \frac{e}{c}\mathbf{A}(\mathbf{r})\right]^2 + V_{dot}(\mathbf{r}) + g^*\mu_B B S_z \ , \tag{1.4}$$

where $\mathbf{p} = -i\hbar\nabla$ and the external magnetic field $\mathbf{B}$ through the vector potential $\mathbf{A}(\mathbf{r})$ [$\mathbf{B} = (\nabla \times \mathbf{A})$] has been introduced. V_{dot} is the effective QD potential seen by the free electrons. μ_B is the Bohr magnetron ($\mu_B = 5.78810^{-2}$meV/T), g^* is the effective g-factor (~-0.4 for GaAs) and m^* the effective mass.

A common way to fabricate doped QDs is to restrict laterally the two dimensional electron gas in a semiconductor heterostructure. The additional in-plane confinement can be achieved by electrostatic gates, or by etching. The typical potentials are schematically shown in Fig. 1.1. The confining potential for electrons along the growth axis (z) is provided by the conduction band profile of the semiconductor heterostructure and typically it is much larger than the in-plane confinement. In this case the potential can be conveniently written as :

$$V_{dot}(\mathbf{r}) = V(z) + V(\rho, \varphi) \ , \tag{1.5}$$

where ρ is the radial coordinate ($\rho^2 = x^2 + y^2$), and $\varphi = arctg(x/y)$.

For QDs like those schematically shown in Fig. 1.1 $V(\rho, \varphi)$ is cylindrically symmetric, leading to conservation of the angular momentum in the growth direction, which represents a good quantum number to classify the electronic states.

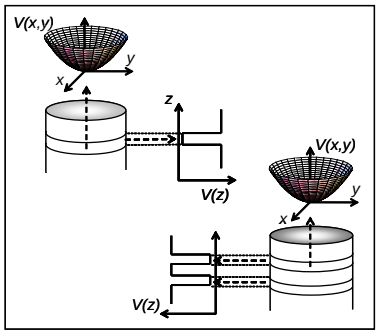

FIGURE 1.1: Representation of the quantum dot potential for single (top) and double (bottom) quantum dots.

In many experimental configurations including the ones addressed in this thesis work, the use of an in-plane parabolic potential [25, 26, 27] is appropriate:

$$V(x,y) = \frac{1}{2}m^*\omega_0^2\rho^2 = \frac{1}{2}m^*\omega_0^2(x^2+y^2) \tag{1.6}$$

where ω_0 is the frequency associated to the in-plane confining potential (see Fig. 1.1).

The parabolic potential of the QDs induced by chemical etching originates from surface states as it will be described in section 3.1.3. It can be anticipated that the experimentally observed in-plane confinement energies are of the order of meV's while the quantum-well confinement energy in the growth direction is of the order of tens of meV. Therefore the separation of the problem as simplified by Eq. 1.5 is justified.

1.1.3 Fock Darwin states

The single particle spectrum of a two-dimensional harmonic oscillator (Eq. 1.6) in a homogeneous magnetic field was first discussed by Fock and Darwin in 1928 and 1930, respectively. The Fock-Darwin (FD) model is a simple conceptual framework for the analysis of single-particle effects in QDs and it represents the basis for more sophisticated approaches.

This section discusses the solution for the in-plane part of the Hamiltonian. In the B=0 case, Eq. 1.4 and Eq. 1.6 lead to the following equation for the in-plane envelope wave-functions of electrons in the conduction band of the parabolic QD:

$$\left[-\frac{\hbar^2}{2m^*}\left(\frac{\partial^2}{\partial x^2}+\frac{\partial^2}{\partial y^2}\right)+\frac{m^*}{2}\omega_0^2(x^2+y^2)\right]\psi(x,y) = \epsilon\psi(x,y)\ . \tag{1.7}$$

Equation 1.7 can be solved by defining the so called *annihilation* operators:

$$a_x = \frac{1}{2}\left(\sqrt{\lambda}\hat{x} + i\frac{\hat{p}_x}{\sqrt{\lambda}\hbar}\right) \quad ; \quad a_y = \frac{1}{2}\left(\sqrt{\lambda}\hat{y} + i\frac{\hat{p}_y}{\sqrt{\lambda}\hbar}\right) \tag{1.8}$$

$$\tag{1.9}$$

where $\hat{x}$ and $\hat{y}$, and $\hat{p}_x$ and $\hat{p}_y$ are the position and the momentum operators in the axial directions, and $\lambda = m^*\omega_0/\hbar$. Defining the number operators as:

$$\hat{N}_x = a_x^+ a_x \quad ; \quad \hat{N}_y = a_y^+ a_y \tag{1.10}$$

where a_x^+ and a_y^+ are the *creation* operators obtained by conjugating a_x, a_y, the Hamiltonian in Eq. 1.7 becomes:

$$H_{xy} = H_x + H_y = \hbar\omega_0(\hat{N}_x + \hat{N}_y + 1) \ . \tag{1.11}$$

By exploiting the cylindrical symmetry of the system, the Hamiltonian can be rewritten in terms of the right and left quanta operators:

$$a_r = \frac{1}{\sqrt{2}}(a_x - ia_y) \quad ; \quad \hat{N}_r = a_r^+ a_r \tag{1.12}$$

$$a_l = \frac{1}{\sqrt{2}}(a_x + ia_y) \quad ; \quad \hat{N}_l = a_l^+ a_l \ . \tag{1.13}$$

It can be shown that these equations lead to a simple form for the Hamiltonian and the angular momentum operators:

$$H = \hbar\omega_0(\hat{N}_r + \hat{N}_l + 1) \tag{1.14}$$

$$L_z = \hbar(\hat{N}_r - \hat{N}_l). \tag{1.15}$$

The actions of a_r (or a_l) on a wavefunction $|\psi_{n_x,n_y}>$ solution of Eq. 1.7, yields a state which is a linear combination of $|\psi_{n_{x-1},n_y}>$ and $|\psi_{n_x,n_{y-1}}>$, that is a stationary state which has one less energy quantum $\hbar\omega_0$ (n_x and n_y are eigenvalues of $\hat{N}_x$ and $\hat{N}_y$, respectively). Similarly the action of a_r^+ (or a_l^+) on $|\psi_{n_x,n_y}>$ yields another stationary state which has one more energy quantum.

Note that the action of the operator a_r^+ yields also a state with an additional angular momentum $\hbar$ (this corresponds to a counterclockwise rotation about the z axis). Similarly, a_l^+ yields a state with an additional angular momentum -$\hbar$ (clockwise rotation). Since L_z commutes with H, the solutions of Eq. 1.14 are also eigenvalues of the angular momentum. These properties can be highlighted in the FD eigen-values by using the n and m radial and azimuthal quantum numbers:

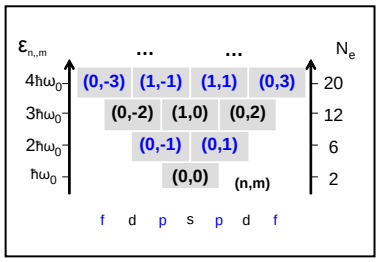

FIGURE 1.2: Fock-Darwin shell structure. The total energy is specified on the left, and the total number of electrons in the dot at full shell occupation is indicated on the right. The atomic-like symmetry of the orbitals is reported in the bottom.

$$\epsilon_{n,m} = \hbar\omega_0(2n + |m| + 1) = \hbar\omega_0(N) \tag{1.16}$$

where $N = (2n + |m| + 1)$ is the shell number, n can take values $n = 0, 1, 2...$ and m, which is also eigen-value of the angular momentum, takes values $m \in \{-(N-1), -(N-2)...0...(N-2), (N-1)\}$. n and m are also given by:

$$n = n_r + n_l \quad ; \quad m = n_r - n_l \tag{1.17}$$

and n_r and n_l are the eigenvalues of the number operators $\hat{N}_r$ and $\hat{N}_l$ defined above.

Figure 1.2 shows the first four FD shells. The FD orbitals are wave-functions with well defined angular momentum, distributed into equally spaced shells with degeneracy given by $2 \times N$, where the factor 2 takes into consideration the spin degeneracy. Each QD electron in the single particle approximation is therefore defined by three quantum numbers n, m, s, or equivalently N, m and s.

Similar to the atomic systems, the first shell is constituted by one s orbital, the second shell by two p orbitals, the third by two d and one s orbitals, etc. Within the single particle picture, the ground state of N_e electrons is formed simply filling the lowest energy shells taking into account the Pauli's exclusion principle only.

Using the cylindrical coordinates ρ and φ, the analytical form for the Fock-Darwin eigenfunctions is:

$$\psi_{n,m}(\rho, \varphi) = \lambda^{(|m|+1)/2} \sqrt{\frac{n!}{\pi(n + |m|)!}} \rho^{|m|} e^{-\lambda\rho^2/2} L_n^{|m|}(\lambda\rho^2) e^{-im\varphi} \tag{1.18}$$

where $L_n^{|m|}(\lambda\rho^2)$ are the Laguerre polynomials.

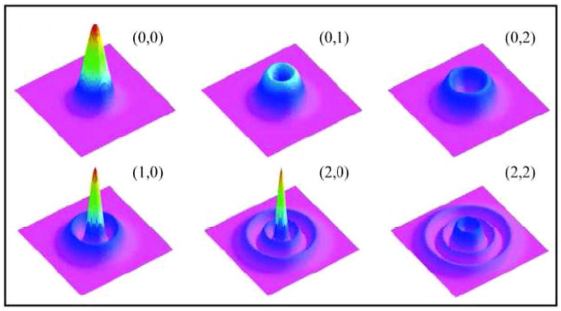

FIGURE 1.3: Wave-functions probability of the Fock-Darwin states for different quantum numbers (n, m).

In this coordinates system:

$$L_z = \frac{\hbar}{i}\frac{\partial}{\partial\varphi} \quad . \tag{1.19}$$

It is straightforward to demonstrate that the Fock-Darwin functions are eigenfunctions of L_z and that:

$$L_z\psi_{n,m} = \hbar m\psi_{n,m} \quad . \tag{1.20}$$

The FD wave-functions corresponding to the lowest six energy FD orbitals, belonging to the first three energy shells are:

$$N = 1 \qquad \psi_{0,0}(\rho,\varphi) = \sqrt{\tfrac{\lambda}{\pi}}e^{-\lambda\rho^2/2} \tag{1.21}$$

$$N = 2 \qquad \psi_{0,\pm1}(\rho,\varphi) = \tfrac{\lambda}{\sqrt{\pi}}\rho e^{-\lambda\rho^2/2}e^{\pm i\varphi} \tag{1.22}$$

$$N = 3 \qquad \psi_{0,\pm2}(\rho,\varphi) = \sqrt{\tfrac{\lambda}{2\pi}}\lambda\rho^2 e^{-\lambda\rho^2/2}e^{\pm i2\varphi} \tag{1.23}$$

$$N = 3 \qquad \psi_{1,0}(\rho,\varphi) = \sqrt{\tfrac{\lambda}{\pi}}(1-\lambda\rho^2)e^{-\lambda\rho^2/2} \quad . \tag{1.24}$$

Figure 1.3 reports the wave-functions probability $\psi^2_{n,m}$ of the Fock-Darwin states for different quantum numbers (n, m).

The mean radius $\left\langle\rho^2\right\rangle_{nm}$ of the FD orbitals is given by:

$$\left\langle\rho^2\right\rangle_{nm} = \frac{1}{\lambda}(2n + |m| + 1) \quad . \tag{1.25}$$

In contrast with squared potentials, in a parabolic QD the mean radius depends on the occupation of the (n,m) orbitals (i.e. on the number of electrons).

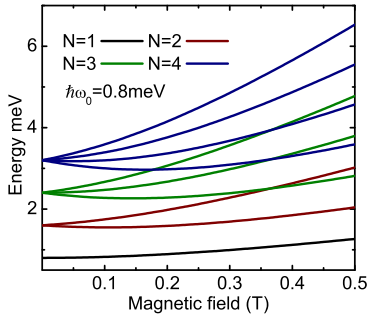

FIGURE 1.4: Evolution of the first four Fock-Darwin shells as a function of magnetic field in the weak field regime. The confining energy $\hbar\omega_0$ is 0.8 meV.

Magnetic field along the growth direction z

This section describes the effect of a magnetic field to the FD orbitals. To this end the *symmetric* gauge is used. In this gauge the vector potential is linked to the magnetic field through:

$$\mathbf{A}(\mathbf{r}) = \frac{1}{2}\mathbf{B} \times \mathbf{r} \tag{1.26}$$

with $\mathbf{B} = B\mathbf{z}$. Note that the *symmetric* gauge is also a Coulomb gauge, i.e.

$$\nabla \cdot \mathbf{A}(\mathbf{r}) = 0. \tag{1.27}$$

Equation 1.4 with the parabolic potential and restricted to the in-plane coordinates becomes:

$$H_0(\mathbf{r}) = \frac{\mathbf{p}^2}{2m^*} + \frac{m^*}{2}\Omega^2\rho^2 + \frac{\omega_c}{2}L_z \tag{1.28}$$

where $\Omega^2 = \omega_0^2 + \omega_c^2/4$ with the cyclotron frequency $\omega_c = \frac{|e|B}{m^*c}$, and L_z is the $\mathbf{z}$ component of the angular momentum defined above. The eigenvalues are given by:

$$\epsilon_{n,m} = \hbar\Omega(2n + |m| + 1) - \frac{\hbar\omega_c}{2}m \ . \tag{1.29}$$

Figure 1.4 shows the energy of the first four Fock-Darwin shells as a function of magnetic field. It can be seen that the magnetic field breaks down the degeneracy of the Fock-Darwin states with the same $|m|$.

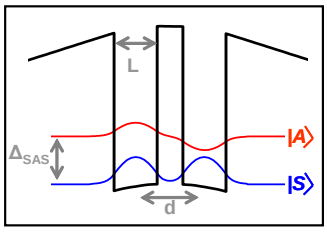

FIGURE 1.5: Schematic representation of the potential profile in the growth direction z of a double quantum dot (DQD). Blue and red curves show the wave-functions along z of the symmetric (S) and antisymmetric (A) states that are separated in energy by the tunneling gap Δ_{SAS}.

The Fock-Darwin wave-functions can be obtained substituting λ with λ^* in Eq. 1.18, where λ^* is given by:

$$\lambda^* = \frac{m^*\Omega}{\hbar} \quad . \tag{1.30}$$

The magnetic field changes the radius of the Fock-Darwin wave-functions from $l_0 = \sqrt{1/\lambda} = \sqrt{\hbar/m^*\omega_0}$ to $l_h = \sqrt{1/\lambda^*} = \sqrt{\hbar/m^*\Omega}$. The average separation between electrons changes with magnetic field, and therefore the Coulomb interaction among electrons.

In the strong magnetic field limit ($l_h < d$) the confining potential in Eq. 1.4 becomes negligible compared to the cyclotron frequency and the two dimensional free-electron behavior prevails over the effect of the confinement leading to the Landau-level energy structure.

1.1.4 Double quantum dots

Double quantum dots (DQD's) can be thought as artificial molecules. They have been considered in several proposals for quantum computation [9, 11, 28] The systems that will be studied in this thesis are vertical coupled dots based on coupled double quantum wells where the lateral confinement is achieved by deep dry etching (section 3.1).

In order to highlight the physics that takes place in the coupled double QD systems, in this section the DQD Hamiltonian is still considered to be separable between the in-plane and growth directions. Figure 1.5 shows the conduction band profile along the z direction where L is the width of both quantum wells and d the inter-well (inter-dot) distance.

The fact that the Hamiltonian is separable in the z and in-plane directions makes the problem along the z direction identical to that in a double quantum

well leading to symmetric and anti-symmetric levels separated by a tunneling gap Δ_{SAS}. Within this approximation the eigen-energies can be written as:

$$\epsilon_{n,m} = \hbar\Omega(2n + |m| + 1) - \frac{\hbar\omega_c}{2}m + 2P\Delta_{SAS} \tag{1.31}$$

where P is a pseudo-spin quantum number that takes values -1/2, 1/2 for symmetric and antisymmetric levels, respectively.

1.2 Many body effects in quantum dots

Within the one-particle approximation discussed above the possible inter-shell excitations from the occupied energy shells occur at discrete and well-defined energies $\Delta N \cdot \hbar\omega_0$. Moreover, in the absence of a magnetic field, the states are spin degenerate and there is no difference between spin and charge excitations as long as they involve the same change in the single-particle shell number. Finally, the intra-shell excitations are not gapped in the single-particle approximation.

When the confinement energy of the QD is sufficiently low and the number of electrons small, the Fermi energy is comparable with the Coulomb interactions and then, similar to what occurs in real atoms, electrons experience interaction effects that lead to significant departures from the one-particle picture presented above.

The simplest correction to the single particle excitation spectra is the exchange interaction that is a consequence of the fermionic nature of the electrons. While the specific stability of the electronic states at "closed shell" occupations 2,6,12,20.. (corresponding to full occupation of the higher occupied shell) is mainly determined by the symmetry of the two dimensional (2D) confinement, the exchange interactions create stable (gapped) configurations at partial occupation numbers. As an example of the impact of the exchange interactions Fig. 1.6 addresses the case of four electrons in a quantum dot. Owing to the exchange energy, the ground state of the system is a triplet with total spin $S = 1$ while the singlet configuration with $S = 0$ is an excited state (S is the sum of all the electron spins S=$\sum s_i$). There exists therefore an intra-shell excitation mode at the finite energy given by the exchange coupling (typically of the order of 1 meV). The impact of this transition is seen in the evolution of the Coulomb blockade spectrum of quantum dots in a magnetic field [15, 29, 30, 31, 32] (see also section 2.1).

These exchange effects can be described by mean-field approximations such as Hartree-Fock. Interaction effects that are not explained by a mean-field approximation are usually referred as correlation.

Correlation effects are particularly significant in condensed matter and they are at the basis of novel electron phases, such as the Wigner molecules predicted

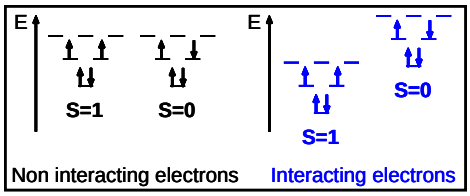

FIGURE 1.6: Comparison of electronic states with total spin $S = 1$ and $S = 0$ in a QD with four electrons. In the non interacting case (in black) both configurations are degenerate. A gap is opened by the exchange term of the many-body interactions.

to occur in QDs [2, 3, 4, 33]. Correlations among electrons are also essential to describe the few-electron QD states proposed as quantum bits (q-bits) for quantum computation. For these reasons the experimental and theoretical analysis of correlations in QDs has been the subject of intense efforts in the last years [1].

From the theoretical point of view, exact diagonalization techniques that are possible to be carried out only in the case of population with few electrons (typically up to 6-7) are the most powerful approaches to describe the QD electronic states beyond a mean-field approximation. Since both Hartree-Fock and exact diagonalization calculations were used to describe the experimental results presented in this thesis, in the rest of this section a schematic description of these approaches is presented.

It is important to note that the radial quantum number n of the the Fock-Darwin levels is no longer a good quantum number of the interacting electron system. As usual, good quantum numbers are defined by the symmetries of the system. In the case of cylindrical QDs the total angular momentum in the z direction M=$\sum m_i$ and the total spin S remain good quantum numbers even in the presence of strong Coulomb interactions.

1.2.1 Hartree-Fock approximations

Mean field approximations including the Hartree-Fock scheme solve the many-body problem by turning the mathematical equations into a single particle problem substituting the real multi-electron potential with an effective one. The Fock-Darwin states can be used as a starting complete orthonormal set of eigen-functions. Variational methods are then exploited to determine the eigen-functions that minimize the energy of the system.

As a first step one may introduce the Hartree approximation, in which the trial function is built as a product of occupied wave-functions:

$$\Psi_0(\mathbf{r}_1, \sigma_1, \mathbf{r}_2, \sigma_2, ..., \mathbf{r}_{N_e}, \sigma_{N_e}) = \phi_1(\mathbf{r}_1, \sigma_1)\phi_2(\mathbf{r}_2, \sigma_2)...\phi_{N_e}(\mathbf{r}_{N_e}, \sigma_{N_e}) \tag{1.32}$$

where Ψ_0 is the trial function for the ground state and $\psi(\mathbf{r})\chi(\sigma) = \phi(\mathbf{r},\sigma)$ where ψ is the orbital part of the Fock-Darwin wave-function and χ is the spin part. The electronic charge density $\rho(\mathbf{r})$ corresponding to the trial wave-function Ψ_0 is:

$$\rho(\mathbf{r}) = -e\sum_{j}^{(occ)}\phi_j^*(\mathbf{r},\sigma)\phi_j(\mathbf{r},\sigma) \ , \tag{1.33}$$

where the sum runs over all occupied spin-orbitals entering the ground state Ψ_0. The Hartree potential corresponding to the charge density above, is given by:

$$V_{coul}(\mathbf{r}) = \sum_{j}^{(occ)}\int \phi_j^*(\mathbf{r}',\sigma)\frac{e^2}{|\mathbf{r}-\mathbf{r}'|}\phi_j(\mathbf{r}',\sigma)d\mathbf{r}' \ . \tag{1.34}$$

The many-body problem is solved adding this effective potential to the original Hamiltonian, which leads to a single variable equation that takes into account the direct Coulomb interactions:

$$\left[\frac{\mathbf{p}^2}{2m^*} + V_{dot}(\mathbf{r}) + V_{coul}(\mathbf{r})\right]\phi_i(\mathbf{r},\sigma) = \epsilon_i\phi_i(\mathbf{r},\sigma) \ . \tag{1.35}$$

The solution is found at convergence of an iterative process.

The Hartree model does not take into account the Pauli's exclusion principle. In this approximation an electron interacts with the total charge density, and therefore also with itself. This includes a non physical energy into the spectrum.

The Hartree-Fock approximation is a more sophisticated mean-field method that is able to introduce the Pauli exclusion principle by using Slater Determinants (SDs) as trial wave-functions:

$$\Psi_0(\mathbf{r}_1,\sigma_1,\mathbf{r}_2,\sigma_2,...,\mathbf{r}_N,\sigma_N) = \frac{1}{\sqrt{N!}}\begin{vmatrix} \phi_1(\mathbf{r}_1,\sigma_1) & \phi_1(\mathbf{r}_2,\sigma_2) & ... & \phi_1(\mathbf{r}_N,\sigma_N) \\ \phi_2(\mathbf{r}_1,\sigma_2) & \phi_1(\mathbf{r}_2,\sigma_2) & ... & \phi_2(\mathbf{r}_N,\sigma_N) \\ ... & ... & ... & ... \\ \phi_N(\mathbf{r}_1,\sigma_1) & \phi_N(\mathbf{r}_2,\sigma_2) & ... & \phi_N(\mathbf{r}_N,\sigma_N) \end{vmatrix} \ . \tag{1.36}$$

Applying the variational principle over the SD it is possible to derive the Hartree-Fock equations:

$$\left[\frac{\mathbf{p}^2}{2m^*} + V_{dot}(\mathbf{r}) + V_{coul}(\mathbf{r}) + V_{exch}(\mathbf{r})\right]\phi_i = \epsilon_i\phi_i \tag{1.37}$$

where the exchange potential is given by:

$$V_{exch}(\mathbf{r})\phi_i(\mathbf{r},\sigma) = -\sum_{j}^{(occ)}\int \phi_j(\mathbf{r}',\sigma)\frac{e^2}{|\mathbf{r}-\mathbf{r}'|}\phi_i(\mathbf{r}',\sigma)d\mathbf{r}'\phi_j(\mathbf{r},\sigma) \ . \tag{1.38}$$

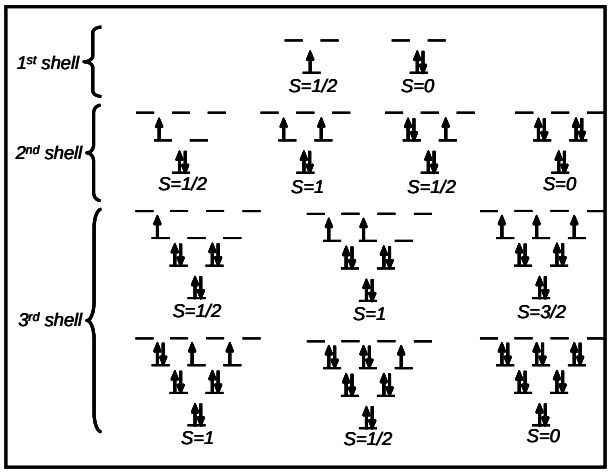

FIGURE 1.7: Preferred electronic configurations in parabolic quantum dots at zero magnetic field at different electron occupation numbers [29, 31, 32].

Hence the exchange potential V_{exch} is a consequence of the Pauli's principle and does not have any classical counterpart. It represents an energy lowering for the system when the electron spins are parallel compared to the case of anti-parallel spin configurations. Within the Hartree Fock approximation, the electrons with parallel spins are kept further apart due to exchange interactions. In addition of modifying the excitation energies, the exchange energy competes with the confinement and kinetic energies in determining the filling of electronic states in QDs.

The impact of exchange interactions is represented by the Hund's rules. Electrons fill the orbitals in a QD maximizing first the total spin and then the total angular momentum. Figure 1.7 represents the shell filling at zero magnetic field at different occupation numbers [15, 29].

1.2.2 Correlated states in quantum dots

The evolution of the energies of the electronic states and excitation spectra in QDs often requires an approach beyond mean-field theories [1]. By correctly taking into account the electron-electron interactions new phenomena arise such as the formation of the so called Wigner molecules, in analogy with the Wigner crystal in bulk semiconductor materials. These interesting effects are predicted to occur in dilute systems where the confining potential is shallow and the number of electrons is small [2, 3, 4, 5, 6].

At high densities i.e., small values of the Wigner-Seitz parameter (in two dimensions $r_s = 1/\sqrt{\pi n}$ with n being the density), the single-particle part of the Hamiltonian Eq. 1.1 dominates over the interactions. In this case, the solutions of mean-field theories compare well with those found with other more accurate methods. Broken-symmetry solutions originating from spatial deformation of the mean field are predicted to occur in QDs for larger values of r_s , i.e., in the correlated regime (Winger crystallization is expected at $r_s \sim 4$). Here, the energies of the electronic states are lower than those of the calculated by mean-field approaches, reflecting the gain in correlation energy.

Interacting electrons confined in a two-dimensional harmonic trap form a seemingly simple many-body problem: if the number of electrons is not too large numerical methods can be applied to solve Eq. 1.1 [1, 34, 35]. These techniques are usually referred as exact because they take into account all the Coulomb effects in equal foot with the non interacting energy states. The accuracy of these methods depends on the possibility to manage large wave-function basis with computational methods. Computational methods typically can calculate electronic states for quantum dots up to 6-7 electrons with reasonable accuracy.

The importance of correlations in these systems was theoretically addressed by G.W. Bryant [2] who highlighted new intriguing properties of QDs triggered by the appearance of new exotic electronic states. For a two-electron system in a long and narrow rectangular box, he studied theoretically the continuous evolution from single-particle-level structure to a regime in which the electron-electron interactions dominate and a Wigner molecule can form. A QD confining two electrons (the so-called *QD helium* [36]) is the simplest example for which the eigenstates and spectra of the two-particle Schrödinger equation can be obtained analytically. For realistic interactions like the Coulomb repulsion, analytic solutions for $N_e > 2$ are impossible to obtain for finite values of r_s.

A well established way to theoretically study a correlated few-electron problem is to apply configuration-interaction methods, which are also frequently used in quantum chemistry. These methods perform numerical diagonalizations of the Hamiltonian using restricted basis [1, 4, 33, 34, 35, 37] and have been used in this thesis work to analyze the experimental results. While a mean field-solution can be expressed as one SD, the solution of the exact diagonalization is always given by a linear combinations of SDs. In the theoretical analysis that will be reported in this thesis work, the SDs are constituted by single-particle Fock-Darwin states. If enough of these states are included in the calculation, the solution converges to the *exact* result and both ground and low-lying excited states are obtained with enough accuracy. The advantage of these methods is that, in addition to the ground-state energy and wave function, all low-lying excitations are computed. This is important, since the excitation spectrum provides insight into the correlated structure of the ground state.

Chapter

2

Survey of experimental studies of electronic states in quantum dots

A review of the experimental achievements in the study of electronic states and intra- and inter-shell electronic excitations in QDs will be presented in this chapter. First single-electron transport experiments in the Coulomb blockade (CB) regime will be discussed. Then optical experiments based on far-infrared absorption and inelastic light scattering will be presented. Since the inelastic light scattering technique will be widely used in this thesis work, the final part of the chapter will introduce the fundamentals of the microscopic theory of inelastic light scattering and the selection rules of this process.

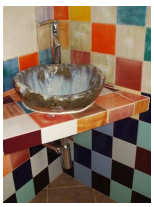

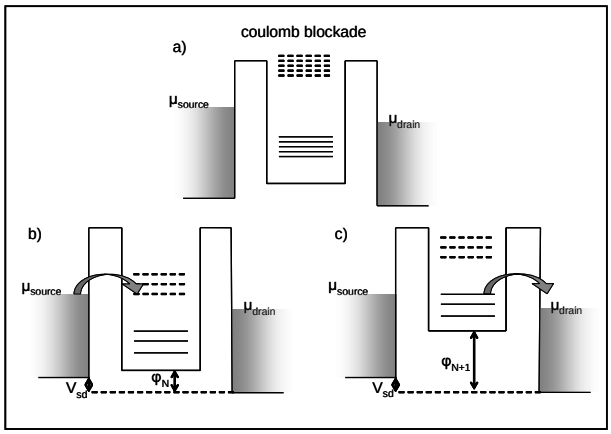

FIGURE 2.1: Representation of the potential landscape that describes charge transport through a QD coupled to two metallic reservoirs. The case of coulomb blockade is shown in (a) while (b) and (c) refer to cases wherein conduction is allowed. Solid lines are occupied electronic states, μ_{source} and μ_{drain} are the chemical potentials of the two contacts. φ_N is the chemical potential of the dot with N_e electrons that can be controlled by a gate voltage.

2.1 Coulomb blockade experiments

The electronic configuration of QD's can be studied in transport experiments. At sufficiently low temperatures, the electronic transport in a QD connected by tunnel barriers to source and drain metallic contacts (as shown in Fig.2.1) is determined by two relevant energies: the charging energy $E_c = e^2/C$ where C is the capacitance of the dot, and the separation ΔE between the quantized energy levels. Transport is affected by E_c if the number of electrons in the dot is well defined. This conditions leads to $E_c \cdot \Delta t = (e^2/C)R_tC >> h$, $R_t >> h/e^2 = 25.813$ KΩ where $\Delta t = R_tC$ is the charging time of the capacitor and R_t the tunnel resistance.

Figure 2.1 shows the potential landscape of a QD along the transport direction. An applied voltage $eV_{sd} = \mu_{source} - \mu_{drain}$ induces a difference between the electrochemical potentials of the two leads. In the case shown in Fig.2.1(a) no states in the dot are available for transport and thus the current is zero (Coulomb blockade CB effect). Alignment of the available QD energy levels with source and drain potentials can be obtained by applying a suitable gate voltage. This leads to the configurations shown in Figs.2.1(b) and 2.1(c) that describe a sequential tunnel process yielding a current peak in the current vs. gate voltage characteristics.

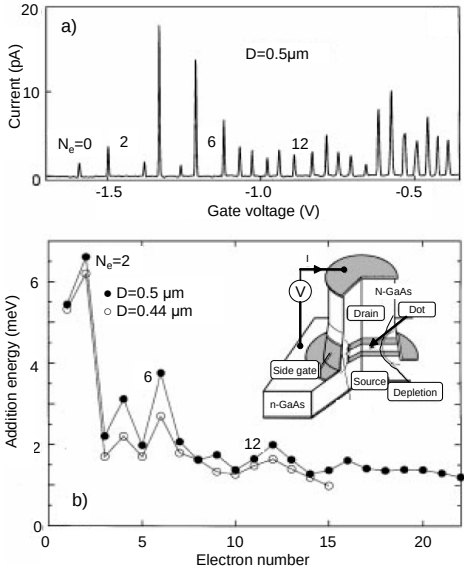

FIGURE 2.2: a) Coulomb oscillations in the current vs. gate voltage at B=0 T observed in a $In_{0.05}Ga_{0.95}As$ quantum dot with a lateral diameter of 0.5 μm. b) Measured addition energy vs. electron number for two dots with different diameters. The inset shows a schematic drawing of the measured devices. Data from Ref. [29].

The addition energy i.e. the energy required to add an extra electron into the dot that leads to the energy level alignment shown in Fig. 2.1(a) is given by:

$$\Delta(N_e) \approx \Delta\epsilon + \frac{e^2}{C} \tag{2.1}$$

with:

$$\Delta\epsilon = \epsilon_{N_e+1} - \epsilon_{N_e} \tag{2.2}$$

where ϵ_{N_e+1} and ϵ_{N_e} are the electronic energies of the dot with $N_e + 1$ and N_e electrons, respectively ($\Delta\epsilon$ is related to ΔE when N_e corresponds to full-shell occupation).

In the many particle regime the transport is dominated by the second term of Eq. 2.1 giving rise to equally spaced peaks in the current vs. gate voltage characteristics. This is due to the small impact of electron-electron interactions and the large degeneracy of Fock-Darwin shells at the Fermi energy. First observations of CB in a nano-fabricated semiconductor device were reported by Meriav et al. [38] in 1990. Soon after those experiments Ashoori et.al. reported first experiments of single electron charging on a GaAs tunnel capacitor containing a single

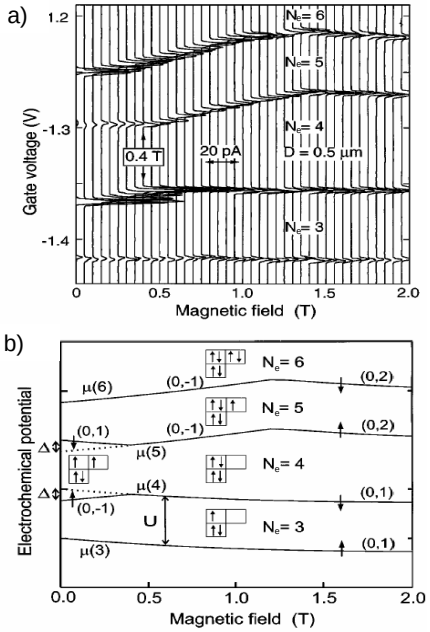

FIGURE 2.3: a) Evolution of the third, fourth, fifth, and sixth current peaks with magnetic field in a QD with D=0.5 μm. N_e is the electron occupation of the dot. b) Calculated electrochemical potential vs magnetic field. Boxes describe schematically the spin configurations. Quantum numbers corresponding to each electronic state (n,m) as described in Fig. 1.2 are also reported. Data from Ref. [29].

microscopic region for charge accumulation [39]. In this device the charge could be varied from zero to few thousands of electrons. Clear observation of electron shell structure in vertical QDs in the regime where $\Delta\epsilon$ is relevant was reported in 1996 by Tarucha et al. [29].

Figure 2.2 (a) shows representative experimental results obtained in the linear transport regime (i.e. $eV_{sd} \longrightarrow 0$) in vertical QDs. The spacing between consecutive CB peaks can be used to determine the addition energy. Figure 2.2(b) shows the measured addition energies vs. electron number. The behavior shown in Fig. 2.2(b) highlights the shell structure of the QD since it demonstrates that larger addition energies are achieved at full shell filling of Fock-Darwin energy levels ($N_e = 2, 6, 12$ electrons) since in these cases $\Delta\epsilon = \hbar\omega_0$ (ω_0 is the confinement energy).

While the appearance of these maxima can be explained within the single-particle FD picture of non interacting electrons, a maximum in the addition

energy at four electrons indicates instead the importance of interaction effects. As anticipated in the previous chapter this effect at $N_e = 4$ is linked to the exchange energy that for 4 electrons favors a triplet ground state configuration (total spin S=1) with respect to the singlet (S=0) configuration with two electrons in the upper shell having spins pointing in opposite directions. Such spin configurations can be studied in more details by applying magnetic fields. Figure 2.3 (a) shows the evolutions of the third, fourth, fifth and sixth current peaks with magnetic field. Figure 2.3 (b) reports the results of calculations based on exact diagonalization methods. In the case of N_e=4 and at zero magnetic field, the ground state is a triplet but it is driven into a singlet state by the impact of the cyclotron energy induced by a magnetic field perpendicular to the plane of the QD. The magnitude of the exchange interaction can be estimated from the value of the magnetic field at the crossover of the two configurations signaled by a shift in the gate voltage position of the current peak (in this experiment $B_c = 0.4$ T yielding an exchange energy $J \sim \frac{\hbar e B_c}{m^* c} \approx 0.7$ meV).

Recently more sophisticated measurements were able to uncover interaction effects using transport measurements in the non linear regime ($V_{SD} > 0$). Ellenberger et.al. [40], for instance, measured the excitation spectrum of a QD with two electrons using non linear tunneling spectroscopy.

Similar transport experiments have been also carried out in symmetric double QDs. In these nano-structures each QD level splits into symmetric and antisymmetric combinations of the states of each QD. Therefore the conduction peaks split into two peaks reflecting the coupling between the energy levels of the two dots [41, 42]. Recent experiments have also addressed the potential impact of two-electron states in double QDs for quantum computation purposes [43].

Despite the successful contribution of transport experiments to the semiconductor QD field, there are two important issues of these approaches that need to be taken into account. First, in transport experiments QDs are coupled to source and drain metallic contacts. Often metallic leads can influence the Coulomb interactions between the electrons in the QD. In addition, transport experiments study QDs as the number of electron changes but they are not able to probe the excitation spectra of the QD without perturbing its charge state.

2.2 Optical spectroscopy in quantum dots.

Optical spectroscopies are widely used methods to study electronic states in semiconductors. This section focuses on spectroscopic techniques that are able to probe *neutral* excitations in the conduction band of semiconductor QDs. The two main methods that will be reviewed here are infrared absorption and inelastic light scattering.

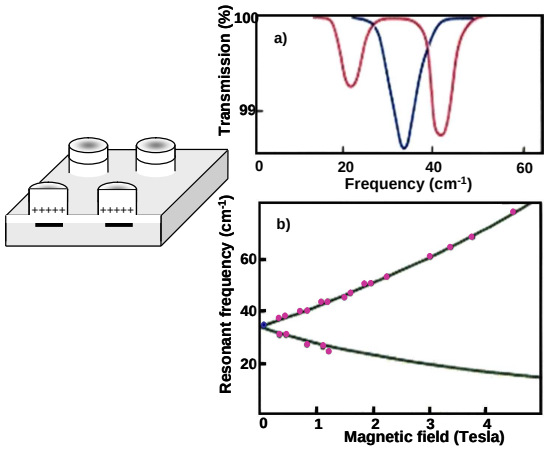

FIGURE 2.4: The cartoon on the left schematically shows shallow-etched QDs. In these dots the etching stops just at the doping layer, and the dot is created by the electrostatic attraction from the donors. a) Transmission coefficient vs. wavenumber showing a single absorption resonance in the absence of magnetic field (blue curve). At finite magnetic field (1.4T) the resonance splits in two peaks (red curve). b) Evolution of the far infrared peaks as a function of the applied magnetic field. The separation is given by the cyclotron energy $\hbar\omega_c$. Data after reference [25].

Inelastic light scattering is particularly powerful because, thanks to its selection rules, it allows to probe both spin and charge neutral excitations. Previous inelastic light scattering experiments performed by three different groups [20, 21, 22] were able to investigate the excitation spectra in nano-fabricated QDs having an electron population of few hundreds. These results will be reviewed in section 2.2.2.

2.2.1 Infrared absorption

The typical energy separation of electronic levels in semiconductor QDs lies in the far-infrared range. At these wavelengths and low temperatures most intrinsic semiconductors are transparent; therefore it is possible to use the absorption of infrared light to probe electronic excitations within the conduction band of doped QDs.

The absorption spectrum of QDs is intimately linked to their potential shape. In vertically-etched QDs, this shape is determined by the charge distribution created by the surface states, and it can be well approximated by a parabolic potential. Absorption experiments in such parabolic potential probe the center-of-mass motion of the electronic system as stated by the Kohn theorem [44, 45, 46].

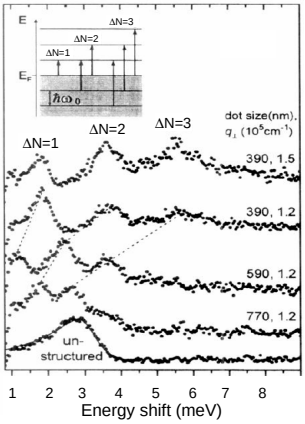

FIGURE 2.5: Resonant inelastic light scattering spectra in QDs with many electrons and different diameters ranging from 390 nm to 770 nm. N is the shell number. After Ref. [21].

Thus in the absence of perturbing potentials (like spin-orbit coupling) far-infrared absorption excites a (dipole) Kohn mode [26, 27], whose energy is not affected by the number of particles and their interactions.

Figure 2.4 reports the far-infrared resonance frequencies due to the dipole intershell electronic excitations ($\Delta N = 1$) in a shallow-etched QD array created by the electrostatic attraction of the dopant layer as schematically shown on the left of Fig. 2.4. The array is composed by many replica of the QD to enhance the optical signal. Figure 2.4(a) shows a single absorption resonance in the absence of magnetic field (blue curve). At finite magnetic field (1.4T) the resonance splits in two (red curve). Figure 2.4(b) reports the evolution of the far infrared peaks of the two resonant modes with separation $\hbar\omega_c$ that increases with applied magnetic field.

2.2.2 Inelastic light scattering

The inelastic light scattering (also referred as electronic Raman) is a process which involves at least two photons. In the Raman Stokes processes like the ones studied in this work, a modulation of charge which oscillates in time is induced by an incoming laser light that is then dispersed at a different wavelength. At first sight one would expect that such experiments would have a very weak signals but taking advantages of the interband resonances of the system it is possible to have peak intensities that in the 2D case can be even stronger than those of the luminescence.

In these resonant inelastic light scattering processes the incident laser light is tuned close to the semiconductor material band-gap (~ 810 nm in GaAs) and creates an inter-band electron-hole pair. In the next step, another electron-hole pair with different energy recombines leaving the system in an excited state. Conservation of energy dictates that the energy difference between the incident and scattered photons corresponds to the energy of the electronic excitations created by the photon field. A representation of the inelastic light scattering process in a QD array is reported in the cartoon of Fig. 2.6. In the backscattering configuration and zero tilt angle ($\theta = 0$) the cylindrical symmetry of the QD allows excitations with even change of the angular momentum ($\Delta M = 0,2,4...$) although it can be proved both theoretical and experimentally that monopole ($\Delta M = 0$) excitations provide the main contribution to the inelastic light scattering signal. At finite tilt angles ($\theta \neq 0$) the symmetry is broken and new excitations such as the dipole $\Delta M = 1$ mode can appear in the inelastic light scattering spectra. Polarization selection rules allow to distinguish between spin and charge excitations. These processes will be studied in section 2.3.

Resonant inelastic light scattering was applied to the study of vertical QDs [20, 21, 22]. These experiments probed the excitations of arrays of QDs each of them containing few hundreds of electrons. An example of the inelastic light scattering signal from QDs with different diameters is shown in Fig. 2.5 [21]. The inelastic light scattering spectra are composed of a series of peaks that can be interpreted as transitions among the QD shells. The multiplicity of the peaks at low energies is regarded as a direct proof of the existence of a shell structure. The spectra are also sensitive to confinement effects as the separation between the peaks increases when the dot diameter decreases.

The right panel of Fig. 2.6 shows another example of light scattering spectra from an array of QDs with a diameter of D = 240 nm and containing many electrons. These experiments highlight that the addition of an in-plane momentum favors the appearance of new peaks corresponding to transitions between states with opposite orbital symmetry such as the dipole (Kohn) mode with $\Delta N = 1$ and $\Delta M = 1$.

Inelastic light scattering from quantum dots with few electrons was reported in the case of an ensemble of self assembled QDs in a InGaAs/AlGaAs system where the number of electrons was changed with a semi-transparent gate [47]. These experiments were able to demonstrate a shift of the inter-shell charge excitations as a function of the electron occupation that was linked to many-body effects. These optical experiments suffered from large inhomogeneous broadening due to size variation from dot to dot so that each individual excitations presented line-widths of the order of several meV that limited the analysis of the electron-electron interaction effects. No spin excitations were reported in those experiments.

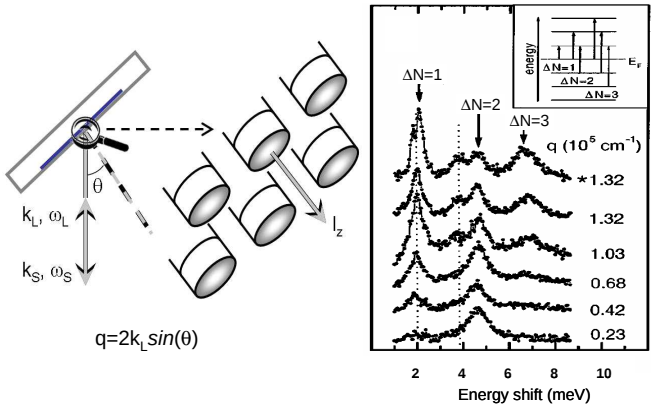

FIGURE 2.6: The cartoon on the left shows schematically the inelastic light scattering geometry. The incident laser light with energy $\hbar\omega_L$ is scattered at energy $\hbar\omega_S$. The transferred in-plane momentum is $q = 2k_L sin\theta$. Right panel: Low temperature inelastic light scattering spectra from an array of D=240 nm QDs populated with many electrons reveal new peaks as the in-plane momentum added to the system increases. Data after Ref. [22].

2.3 Microscopic mechanisms of inelastic light scattering in quantum dots

This section provides the fundamentals of the theoretical description of the inelastic light scattering process by electrons confined in QDs. To this end the system of QDs plus the electromagnetic field is described with the following Hamiltonian:

$$H = H^{(e)} + H^{(rad)} + H_{int} \ , \tag{2.3}$$

where $H^{(e)}$ and $H^{(rad)}$ are the Hamiltonians of the electronic states and of the (quantized) photonic field, respectively and H_{int} is the light-matter interaction term. Treating this last term as a perturbation is valid unless the electronic system is strongly coupled to the radiative one (like in an optical cavity or a photonic crystal). The experiments described in this work are modeled using this approximation. The framework for the calculation of the Raman cross-section is based on second-order perturbation theory. The linear and quadratic terms in the vector potential $\mathbf{A}$ of the electromagnetic field entering in the Hamiltonian above are:

$$H_{int} = H^{A}_{int} + H^{A^2}_{int} = \frac{1}{2m}\sum_i e\mathbf{A}(\mathbf{r}_i)\cdot\mathbf{p}_i + \mathbf{p}_i\cdot\mathbf{A}(\mathbf{r}_i) + e^2|\mathbf{A}(\mathbf{r}_i)|^2 \ , \tag{2.4}$$

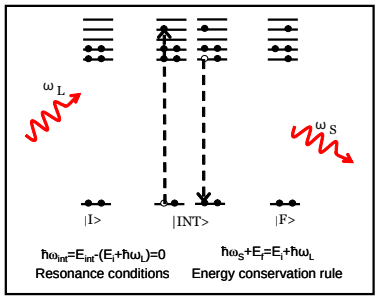

FIGURE 2.7: Schematic representation of the microscopic mechanism of the inelastic light scattering process described by the second term in Eq. 2.6. The initial state with N_e electrons in the ground state and a distribution of photons with $\hbar\omega_L$ is converted into an intermediate state with an electron-hole pair through the annihilation of one of the photons. The final state is an excited state of the N_e electrons and a photon with energy $\hbar\omega_S$.

where e is the electron charge, and $\mathbf{p_i}$ is the momentum of the i^{th} electron while m is the electron mass in vacuum.

The probability of a transition from an initial collective state Ψ_I to a final collective state Ψ_F is:

$$C_{FI} = \frac{e^{i(\hbar\omega_S + E_F - \hbar\omega_L - E_I)t/\hbar} - 1}{\hbar\omega_S + E_F - \hbar\omega_L - E_I} \cdot A_{FI} \ , \tag{2.5}$$

where $E_{I,F}$ refer to the energies of the initial and final electronic states, $\omega_{L,S}$ are the frequencies of the incident laser and scattered lights. The matrix element A_{FI} is:

$$A_{FI} = -\left\langle \Psi_F \left| H_{int}^{A^2} \right| \Psi_I \right\rangle + \sum_{\Psi_{INT}} \frac{\left\langle \Psi_F \left| H_{int}^{A} \right| \Psi_{INT} \right\rangle \left\langle \Psi_{INT} \left| H_{int}^{A} \right| \Psi_I \right\rangle}{\hbar\omega_{INT}} \ , \tag{2.6}$$

with $\hbar\omega_{INT} = E_{INT} - (E_I + \hbar\omega_L)$, where $E_{INT} - E_I$ is the difference between the total energies of the intermediate and initial states. The total wave-function $|\Psi_I\rangle$ is taken as a product of the photon field and the many-body electronic functions $|I\rangle$. Same holds for the final and intermediate states. The sum runs over all possible intermediate states and the differential cross section can be computed integrating the transition probability on time:

$$\frac{d\omega}{d\Omega_F d\omega_F} \sim \sum_F \int |C_{FI}|^2 \, dt = \sum_F |A_{FI}|^2 \, \delta\left(E_I + \hbar\omega_L - E_F - \hbar\omega_S\right) \tag{2.7}$$

where $d\Omega_F$ is the element of solid angle related to the wave-vector of the scattered photon.

The first term in the right-hand side of in Eq. 2.6 incorporates electronic initial and final states that are both in the conduction band. Thus it can be evaluated without taking into account the valence band and takes the form of the structure factor [19] of a system of charged particles. This response can be seen with parallel incoming and outgoing light polarizations. However, the experiments described in this thesis are all performed in resonance conditions, in which the second term in A_{FI} gives the dominant contribution.

The second term in the right-hand side of Eq. 2.6 is particularly relevant since it includes a resonant factor in the denominator that resonates when $\hbar\omega_L = E_{INT} - E_I$. This term provides the main contribution to the cross section of the resonant Stokes light scattering described in Fig. 2.7: in the initial configuration the system is made of N_e electrons in the conduction band in the ground state and a number of photons with energy $\hbar\omega_L$ tuned close to the the semiconductor gap. Then the creation of an electron-hole pair across the band-gap annihilates a photon. Finally another electron-hole pair with different energy recombines emitting a photon with energy $\hbar\omega_S$. This last process leaves the electronic system with N_e electrons in the conduction band in an excited state populated by a collective neutral excitation. The δ function in Eq. 2.7 dictates the conservation of energy between the initial and final states, i.e. $\hbar\omega_S + E_F = E_I + \hbar\omega_L$.

2.3.1 Polarization and parity selection rules

Selection rules and matrix elements entering the second term of A_{FI} are now discussed. Detailed calculations of the Raman cross-sections can also be found in references [24, 33, 34, 35, 48, 49]. In second quantization formalism the linear term in $\mathbf{A}$ of H_{int} entering in Eq. 2.6 takes the following form:

$$H^A_{int} = \frac{e}{m}\sum_k \sum_{\alpha,\beta} \left\{ \left\langle \alpha \left| e^{i\mathbf{kr}} \epsilon_k \mathbf{p} \right| \beta \right\rangle a_k e^+_\alpha e_\beta + \left\langle \alpha \left| e^{-i\mathbf{kr}} \epsilon^*_k \mathbf{p} \right| \beta \right\rangle a^+_k e^+_\alpha e_\beta \right\} \tag{2.8}$$

where $\mathbf{k}$ is the photon wave-vector, $\mathbf{p}$ is the dipole momentum operator, $\epsilon_\mathbf{k}$ is the light polarization vector, α, β refer to all possible one-particle electronic states in the conduction and valence bands of the QD. The one particle electronic states α and β are given by the product of Bloch function times an envelope function [1]. The notation a^+_k, a_k (e^+_α, e_α) refers to the photon (electron) creation and annihilation operators, respectively. For example, the first term in Eq. 2.8 represents the absorption of a photon with the destruction of an electron in state β and the creation of an electron in the state α. The sum over all α, β states carries all the information about the QD absorption properties.

[1] In the theoretical calculations reported in Chapter 5 the envelope function is determined from the solution of the Kohn-Sham Hamiltonian as also described in reference [35]

The calculation of the resonant terms in Eq. 2.6 thus takes into account the electronic states in the valence band that appear as intermediate states. These states are crucial for the observation of spin excitations since the spin-orbit coupling of p-like states in the valence band produces states of mixed spin and orbital character. Further mixing of the valence band states is induced by the lateral confinement of the QD [23].

In the effective mass formalism hole states of QDs in the valence band are defined by the product $\varphi_\beta(r) \cdot u^j_{m_j}(r)$ where $\varphi_\beta(r)$ is the envelope orbital function and $u^j_{m_j}(r)$ are the representations in the direct space of the Bloch functions. j, m_j refer to the total angular momentum index $j = l + s$ and its projection in the z direction respectively. Calculations of Raman cross-sections in QDs can be carried out using the Luttinger Hamiltonian that describes the mixing of hole states in QDs [24]. Here only a single valence band with m_j that can take values between $-3/2$ and $3/2$ will be used (as in reference [35]). Following this approximation the holes can be labeled using $|\beta, m_j>$, while the electronic functions α will be specified by $|\alpha, \sigma\rangle$ (where the spin σ can take values 1/2 and -1/2 labeled with $\uparrow$ and $\downarrow$, respectively).

Considering initial states with photons at energy $\hbar\omega_L$ and final states where one of these photons is replaced by a photon at energy $\hbar\omega_S$, the photon terms can be computed arriving to the following equation:

$$A_{FI} \sim \sum_{INT} \frac{\left\langle F \left| H^+_{e-r} \right| INT \right\rangle \left\langle INT \left| H^-_{e-r} \right| I \right\rangle}{\hbar\omega_{INT}} \ , \tag{2.9}$$

where $|I\rangle$ and $|F\rangle$ now describe the electronic collective states of the QD in the conduction band that may be expressed as a sum of SD built with Fock-Darwin functions.

In order to derive the selection rules the energy variations between different intermediate states ($E_{int} - E_i - \hbar\omega_L \approx E_{gap} - \hbar\omega_L$) are neglected. Using the completeness relation for the intermediate states, Eq. 2.9 becomes:

$$A_{FI} \sim \frac{\left\langle F \left| H^+_{e-r} H^-_{e-r} \right| I \right\rangle}{E_{gap} - \hbar\omega_L} \tag{2.10}$$

A_{FI} has terms that contribute to charge and spin excitations. For example the term corresponding to a spin transition can be written as:

$$[\uparrow\downarrow] \sim \sum_{m_{j'}\bar{\gamma}} \left\langle \alpha \uparrow \left| e^{i\mathbf{k}_S\mathbf{r}} \epsilon_F \cdot \mathbf{p} \right| \bar{\gamma}, m_j \right\rangle \left\langle \bar{\gamma}, m_j \left| e^{-i\mathbf{k}_L\mathbf{r}} \epsilon^*_F \cdot \mathbf{p} \right| \alpha' \downarrow \right\rangle \left\langle F \left| e^+_{\alpha\uparrow} e_{\alpha'\downarrow} \right| I \right\rangle \tag{2.11}$$

Similar terms describe the spin configurations [$\uparrow\uparrow$], [$\downarrow\uparrow$], [$\downarrow\downarrow$] that enter in

σ / m_j	3/2	1/2	- 1/2	- 3/2
1/2 [↑]	ϵ_+	$\sqrt{2/3}\,\epsilon_z$	$\sqrt{1/3}\,\epsilon_-$	0
-1/2 [↓]	0	$\sqrt{1/3}\,\epsilon_+$	$\sqrt{2/3}\,\epsilon_z$	ϵ_-

TABLE 2.1: Matrix elements of factors $\epsilon \cdot \mathbf{p}$ depend only on the electron spin projection σ on the hole index m_j. In this table the matrix elements $\frac{\langle \sigma|\epsilon\cdot\mathbf{p}|m_j\rangle}{i}$ are computed, where $\epsilon_\pm$ are defined as $\epsilon_\pm = \mp\frac{(\epsilon_x \mp i\epsilon_y)}{\sqrt{2}}$. The details of how to calculate the hole elements with the Luttingher-Kohn Hamiltonian can be found in reference [24].

Eq. 2.10. The matrix elements $\frac{\langle \sigma|\epsilon\cdot\mathbf{p}|m_j\rangle}{i}$ are reported in table 2.1 where the components $\epsilon_\pm$ are defined as $\epsilon_\pm = \mp(\epsilon_x \mp i\epsilon_y)/\sqrt{2}$.

After computing the possible transitions in Eq. 2.9 using table 2.1. A_{FI} reads as follows:

$$A_{FI} \sim \sum_{\alpha,\alpha'} \left\langle \alpha \left| e^{i(\mathbf{k}_L - \mathbf{k}_S)\cdot\mathbf{r}} \right| \alpha' \right\rangle \cdot \tag{2.12}$$

$$\cdot \left\langle F \left| \left\{ \frac{2}{3}(\epsilon_I \cdot \epsilon_F)\left[e^+_{\alpha\uparrow}e_{\alpha'\uparrow} + e^+_{\alpha\downarrow}e_{\alpha'\downarrow}\right] + \frac{i}{3}(\epsilon_I \times \epsilon_F)\cdot\hat{z}\left[e^+_{\alpha\uparrow}e_{\alpha'\uparrow} - e^+_{\alpha\downarrow}e_{\alpha'\downarrow}\right] \right.\right.$$
$$\left.\left. + \frac{i}{3}(\epsilon_I \times \epsilon_F)\cdot(\hat{x} + i\hat{y})e^+_{\alpha\uparrow}e_{\alpha'\downarrow} + \frac{i}{3}(\epsilon_I \times \epsilon_F)\cdot(\hat{x} - i\hat{y})e^+_{\alpha\downarrow}e_{\alpha'\uparrow} \right\} \right| I \right\rangle$$

where α, α' refer to orbital one-electron states in the conduction band since the Bloch terms have been computed together with the spin.

The first operator proportional to $(\epsilon_I \cdot \epsilon_F)$ connects states with equal spin ($\Delta S = 0$). This Raman term corresponds to charge excitations. The other three operators proportional to $(\epsilon_I \times \epsilon_F)$ correspond to spin excitations that can be seen when the the incoming and outgoing polarization directions are orthogonal. These excitations are linked to a change of the total spin of $\Delta S = \pm 1$. Two kinds of spin excitations can be distinguished: the second operator in the second line is seen when the incoming and outgoing polarizations are within the plane perpendicular to the QD growth axis z. It corresponds to a spin-density excitation with $\Delta S = \pm 1$ and $\Delta S_z = 0$. The last two operators are instead spin-flip excitations ($\Delta S = \pm 1$ and $\Delta S_z = \pm 1$) and need at least one component of the polarization vector of the incoming or scattered light along the axis of quantization of spin that in our notation corresponds to the z direction. Spin-flip excitations are not seen in a back-scattering configuration that corresponds to an incidence angle $\theta = 0$, which is the most used experimental geometry in this thesis work.

The orbital part written in the first line of Eq. 2.12 provides the multi-pole or parity selection rules. The wave-vector transfer during the light scattering process is very small, and determined by the aperture of the collecting lenses (more experimental details will be given in the following chapter). In this geometry $\mathbf{k_L} - \mathbf{k_S} \approx 0$. The Taylor expansion of the function $e^{i(\mathbf{k}_L - \mathbf{k}_S)\cdot\mathbf{r}}$ leads to sum of multi-pole factors. The main term for the expansion of the orbital part in Eq. 2.12 leads to a monopole which is proportional to:

$$A_{FI}^{0} = \left\langle F \left| \sum_{\alpha,\alpha'} \left\langle \alpha \left| \rho^2 \right| \alpha' \right\rangle \left[e_{\alpha\uparrow}^{+} e_{\alpha'\uparrow} + e_{\alpha\downarrow}^{+} e_{\alpha'\downarrow} \right] \right| I \right\rangle \tag{2.13}$$

i.e. the matrix element of the monopole operator (leading to the selection rule $\Delta M = 0$ at $\theta = 0$), where ρ, θ are polar coordinates in the plane.

Finally it can be noted that A_{FI}^{0} depends on the overlap between the initial and final states. The wave-functions are more spatially extended for high energy states. The overlap between the ground and excited states decreases when the energy difference between them increases. Thus the matrix elements A_{FI}^{0} tend to be smaller for excitations at higher energy. Examples of calculated inelastic light scattering spectra and comparison with experimental data will be reported in chapter 5.

Theoretical evolution of spin excitations

The spin and charge intershell excitations are shifted from the single particle excitations due to dynamical many-body interactions. Such single-particle excitations have been studied extensively in the 3D [51] and in the 2D cases. In 2D they appear as a sharp peak in the Raman spectra of intersubband excitations between the intersubband spin and charge density excitations at an energy corresponding to the intersubband splitting [18]. Figure 2.8 shows the dipole strength function of the $\Delta N = 2$, $\Delta M = 0$ spin mode (black curves) of QDs with a confinement potential $\hbar\omega_0 = 2.78$ meV with different numbers of electrons (N_e=5, 25 and 210). The calculations were performed by Serra et.al. [50] using a local-spin-density functional theory that includes the direct and exchange Coulomb interactions. Black lines represent the spin channel while red lines represent the free-particle strength function which are seen under resonance conditions. As it can be observed in Fig 2.8, the red-shift of the spin mode from the single-particle transition is seen at the low electron occupation but it collapses to zero as the electron number is increased (more shells are occupied). This effect indicates a cancellation of the dynamical exchange-correlation corrections that occurs where many electronic shells are occupied. This effect is equivalent to what occurs in the 2D case when many sub-bands are occupied [52].

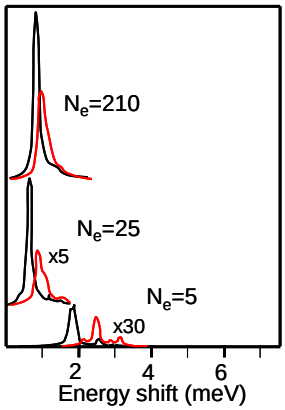

FIGURE 2.8: Calculated dipole strength function of the $\Delta N = 2$ $\Delta M = 0$ mode of QDs with a confinement potential $\hbar\omega_0 = 2.78$ meV containing a different number of electrons (N_e=5, 25 and 210). Black lines represent the spin channel while red lines represent the free-particle strength functions. Data after reference [50].

Excitations in the conduction band of quantum dots

This section summarizes the inelastic light scattering processes and the involved electronic states that are relevant for the interpretation of the experiments presented in the following chapters.

To this end Fig. 2.9 shows the possible transitions that can be probed by inelastic light scattering in the case of QDs with four electrons. The ground state of QDs with four electrons dictated by Hund's rule is a triplet with total spin S=1.

The exact collective states in QDs can be described by an infinite series of SD constructed from Fock-Darwin states, as shown in Fig. 2.9(a). In this panel the excited state is represented by a combination of SD. In the other panels of Fig. 2.9 the electronic states are represented showing only the most representative electronic configuration as obtained by exact diagonalization calculations [34].

As mentioned above, inelastic light scattering can probe collective spin ($\Delta S = \pm 1$, in black) and charge ($\Delta S = 0$, in red) excitations detected in perpendicular and parallel light polarizations, respectively. In the back-scattering configuration with normal incidence, inter-shell monopole excitations ($\Delta N = 2, \Delta M = 0$) like the one described in Figs. 2.9 (a), (b) and (c) dominate the inelastic light scattering signal. The mode described in Fig. 2.9(d) is instead an intra-shell excitation ($\Delta N = 0$) between spin configurations separated by the exchange interactions only. Fig. 2.9 (e) represents the quadrupole charge inter-shell excitation. Quadrupole

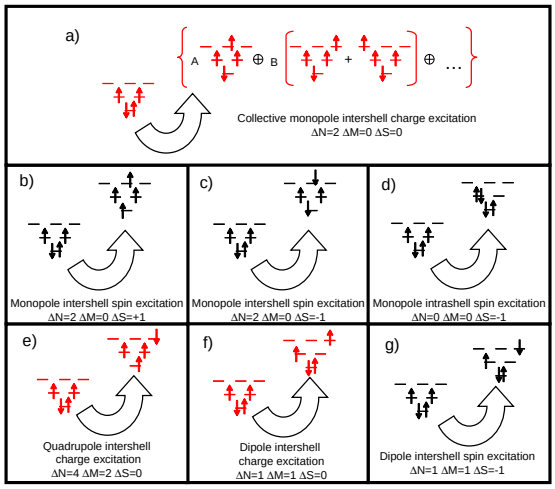

FIGURE 2.9: Representation of the possible transitions accessible by inelastic light scattering in a QD with four electrons. Spin and charge excitations are depicted in black and red respectively. In (a) the exact excited state is represented by a combination of SD. The coefficients A,B... can be evaluated by exact diagonalization methods [34]. In the rest of the figure the electronic states are represented showing only the most representative electronic configuration. The quantum numbers that describe such excitations are reported in the bottom of each panel.

excitations are allowed by symmetry selection rules. Calculations of the cross-sections of these transitions, however, reveal that quadrupole modes are much weaker than monopole excitations [53].

The addition of an in-plane wave-vector to the system allows higher-order excitations in angular momentum ($\Delta M \neq 0$) to be probed. Those are described in Fig. 2.9(f) and (g). While dipole charge excitations shown in Fig. 2.9(f) can be detected in absorption experiments, the dipole spin excitation like the one displayed in Fig. 2.9(g) is not accessible by this method.

Chapter

3 Fabrication methods and spectroscopy techniques

Samples, fabrication methods and experimental set-ups used for the spectroscopic study of dry etched QDs are presented in this chapter. The main techniques used for the QD fabrication are electron beam lithography and reactive ion etching. They have been chosen because of their great flexibility in the realization of QDs with the desired shapes. For the light scattering studies of these QDs an optimized optical set-up with superb spectral resolution and signal sensitivity is required. This will be presented in the last part of the chapter.

3.1 Fabrication of arrays of identical quantum dots

The inelastic light scattering signal provided by few electrons in a single QD is expected to be extremely weak. In order to increase the signal the strategy employed in this work is to study arrays of identical dots. However the preparation of these arrays is very delicate. Arrays containing 10^4 identical (same metallurgical dimensions) nano-fabricated AlGaAs/GaAs pillars were prepared. Each pillar contains a (two dimensional) doped QD based on a modulation-doped semiconductor heterostructure. The three key ingredients for the successful fabrication of these QDs are the following:

- High-mobility two dimensional electron gases (2DEG). To this end, high quality samples with electron mobility above 10^6 cm^2/Vs were used.
- High-resolution lithography (below 20 nm) in an extended area (100×100 μm).
- Low-damage dry etching that minimizes the penetration depth of the etching ions.

The steps followed for the fabrication of homogeneous arrays of high quality QD's are now presented. More details about the recipes used in the lithography and etching processes are reported in Appendix A.

3.1.1 Quantum well samples

The substrates used in this thesis work were grown by molecular beam epitaxy (MBE) using the modulation doping technique. MBE allows atomic control in the sequence of layers while modulation doping assures high electron mobility and permits to control the amount of charge. Samples were grown by Loren Pfeiffer and Ken West at Bell Laboratories in Murray Hill (NJ, USA) and by Lucia Sorba and Giorgio Biasiol at TASC labs (Italy).

Single and a double quantum wells (QWs) samples were used for the fabrication of the QDs used in this work.

Single quantum dot substrate

A one-side modulation-doped QW was used as substrate for the fabrication of single QDs. The cartoon in Fig. 3.1 shows the sequence of layers grown by MBE. The QD originates from the lateral confinement of the 2DEG confined in the 25 nm wide, $Al_{0.1}Ga_{0.9}As$/GaAs QW located 180 nm below the surface. The δ-doped layer between the surface and the QW has a high content of Si, so that the donor atoms are not completely ionized; this assures a lower disorder

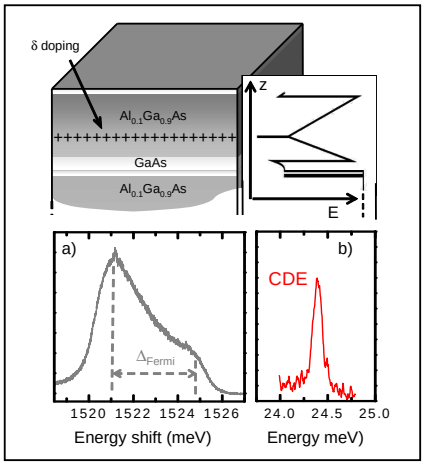

FIGURE 3.1: The cartoon on top represents the sequence of layers grown by MBE that creates the high mobility 2DEG. The calculated conduction band profile in the growth direction is also shown. A 2DEG with electron density $n_e = 1{,}1\times10^{11}$ cm^2 and carrier mobility of $2{,}7\times10^6$ cm^2 / Vs is realized in the QW. a) Low temperature (T=1.9K) luminescence spectrum from the QW 2DEG. b) Low temperature (T=1.9K) inelastic light scattering spectrum with parallel polarizations of the incoming and scattered photons. The peak is assigned to the QW inter-subband charge density excitation (CDE).

because of the screening effect due to the pinning of the Fermi energy at the bottom of the conduction band at the δ doping layer. In this way the QW is not affected by surface states occurring at the semiconductor/air interface. This δ-doping is separated from the QW by a spacer of 60 nm. The low content of Al used in the barriers of these samples minimizes alloy fluctuations and possible impurities transferred into the QW during the growth process. The calculation of the conduction band profile using a Poisson-Shrödinger program is shown in Fig. 3.1. The measured low-temperature electron density is $n_e = 1{,}1\times10^{11}$ cm^{-2} and the carrier mobility is $2{,}7\times10^6$ cm^2 / Vs. The low electron density allows to achieve the few electron regime at reasonable QD diameters.

The photo-luminescence (PL) spectrum shown in Fig. 3.1(a) manifests the typical emission line due to electron-hole recombinations of electrons from the bottom of the conduction band up to the Fermi energy (E_F). The absence of excitonic features is attributed to the very efficient screening effects of the 2DEG and the low density of defects. The width Δ_{Fermi} of the emission line (the energy separation between the luminescence peak intensity associated to the optical recombination of electrons at the bottom of the conduction band and the shoulder due to recombination of electrons at the Fermi level) can be linked to the

electronic density using the relation:

$$\Delta_{Fermi} = E_F \frac{m_e^* + m_h^*}{m_h^*} = 8\pi\hbar^2 n_e \cdot \frac{m_e^* + m_h^*}{m_e^* m_h^*} \tag{3.1}$$

where m_e^* and m_h^* are the electron and hole effective masses, respectively. In the case of this sample $\Delta_{Fermi} \approx 4$ meV yielding an electron density of $n_e \approx 1{\times}10^{11}$ cm^2, in agreement with the magneto-transport experiments. Figure 3.1(b) reports a representative resonant inelastic light scattering spectrum with parallel incoming and outgoing polarizations. The peak is assigned to the QW intersubband charge density excitation (CDE) [18]. The sharp linewidth of the CDE peak ($\sim$ 0.1 meV) demonstrates the optical quality of the heterostructure. The energy scale for the lateral QD confinement is expected to be in the range of few meV or less [20, 21, 22]. The data reported in Fig. 3.1(b) show that the intersubband energy separation due to the confinement in the vertical direction is instead of the order of few tenths of meV. This justifies the separation of the QD Hamiltonian in the in-plane and growth directions as done in section 1.1.2.

Double quantum wells

The double QW used for the fabrication of double QDs consists on two identical 18 nm-thick GaAs QWs separated by an $Al_{0.1}Ga_{0.9}As$ barrier of 6 nm. The double QW is symmetrically-doped. Low aluminum concentration was used as in the single QW case to improve the quality of the sample. The double QW structure starts 400 nm below the surface. In order to assure the symmetry of the profile, a δ-doping layer was grown close to the surface to avoid surface effects. The low-temperature electron density and mobility measured from Shubnikov De Haas are $n_e = 3 \times 10^{11}$ cm^{-2} and $\mu = 2.7 \times 10^6$ cm^2/Vs, respectively.

Coupling between the QW's results in energy splitting between symmetric and antisymmetric combinations of the QW states of the individual QWs. The energy difference is the tunneling gap Δ_{SAS} (see section 1.1.4). Δ_{SAS} is estimated from inelastic light scattering measurements to be $\approx$ 0.8 meV. Luminescence measurements marked the electron-hole recombination from the bottom of the conduction band to the top of the valence band at $\sim$ 1527 meV.

3.1.2 Realization of vertical QD arrays

The lateral QD confinement was achieved using a combination of electron beam lithography (e-beam) and reactive ion etching (RIE). Arrays of QDs of dimensions 100 μm $\times$ 100 μm with a 1 μm period were designed in order to maximize the light scattering signal. The dot separation of 1μm was chosen to avoid interdot coupling and to allow the study of single dot photoluminescence.

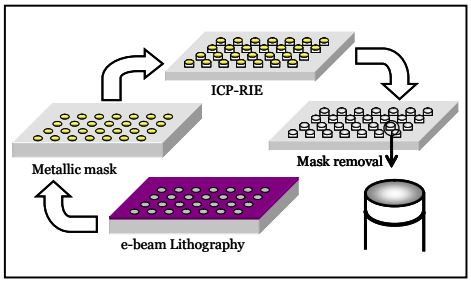

FIGURE 3.2: Schematic representation of the QD's fabrication process. First a pattern of holes is defined in a Poli Metil Metacrilato (PMMA) layer using electron beam lithography. Then Ni is evaporated and after lift-off an array of metallic disks is realized. The dry etching process (inductive coupled plasma reactive ion etching ICP-RIE) defines pillars underneath the metallic disks. The metal is removed from the sample using a selective wet etching.

The optimization of the fabrication methods that are schematically shown in Fig. 3.2 was essential to achieve the required quality of the nano-structures for the observation of few-electron effects by inelastic light scattering. In the following paragraphs the protocols used in this thesis work will be schematically presented.

Mask fabrication

The definition of the dot pattern required for the etching process consisted in three steps: the electron beam lithography, the evaporation of the metal, and the lift off. The advantage of modern e-beam lithography is that it allows to control the shape and the position of the dots which are essential characteristics looking forward to future applications. The spatial definition achieved was below 20 nm in an area of 100 μm×100 μm. After the lithography step a Ni evaporation was used to define the mask. Ni is a hard metal resistant to the etching process, and it can be easily removed with the appropriate selective wet etching. Details on the fabrication methods used in this work are reported in Appendix A.

Inductive coupled plasma

The achievement of anisotropic profiles that could etch through the 2DEG's, leading to deep-etched QDs requires dry-plasma processes. A major issue with AlGaAs/GaAs nano-structures with low electron density and fabricated by dry etching is that surface damage is very detrimental to their optical process. In particular QDs are very demanding due to their small dimensions. During this work two different plasma reactors, capacitively coupled reactive ion etching

FIGURE 3.3: SENTECH SI500-PTSA plasma etcher at the NEST laboratories in Pisa. The Planar Triple Spiral Antenna is shown in the inset to the picture.

(RIE), and inductive coupled plasma RIE (ICP-RIE) [54, 55] were used. However RIE suffers from limitations to fabricate very small devices since it leads to a high density of etching defects that are created on the lateral side-walls of the QD. These limitations become specially relevant on samples with aluminum content since $Al_xGa_{1-x}As$ is harder than GaAs and requires higher energy plasmas.

ICP sources are able to operate at lower pressures (1-20mTorr) producing high density plasmas (1×10^{11} to 1×10^{12} ions cm^{-3}). In a ICP etcher the ion energy incident on the sample can be decoupled from the plasma generation. Plasma densities are typically a factor 10-100 times higher than those achieved in capacitive dischargers. As a result, these sources are capable of etching anisotropic features at high rates with low power.

The ICP machine used in this work was a SENTECH SI-500 PTSA (planar triple spiral antenna) ICP plasma etcher shown in Fig. 3.3. This system differs from other plasma etchers by the use of the PTSA designed to obtain low damage, high aspect ratio, and high etching rates in III-V semiconductor. Samples were mounted in a Si carrier wafer with vacuum oil to ensure good heat transfer. The wafer was clamped to the cathode and cooled by helium gas on the backside. The triple antenna ionizes the molecules and creates the plasma and then the ions are accelerated into the sample applying a radio-frequency power to the wafer chuck. The optimal recipe to etch GaAs/AlGaAs consists in a mixture of BCl_3, Cl_2 and Ar gases.

The etching protocol used for the samples in this thesis enabled the realization of QDs with almost vertical walls, although a slight undercut was present for

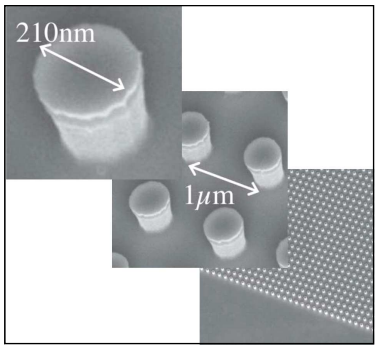

FIGURE 3.4: Scanning electron microscope pictures of fully processed quantum dots with D = 210 nm. The panel at the bottom right demonstrates the high homogeneity achieved. The other panels display single QDs.

the smallest samples. The aspect ratio in these dots is 2/5. The metallic mask was removed at the end of the etching process using a solution of FeCl-H_2O-HCl. The etching selectivity was 1-200, and the etching rate in the Ni mask was faster than 2nm/s.

The etching process was carried out through all the active part of the structure, i.e. below the 2DEG in the case of single dots, and below the last doping layer in the case of double QDs. This is usually referred as deep etching in contrast with shallow etching where the etching stops at the donors level and the QD is formed by the electrostatic attraction of the remaining donors to the free carriers in the QW (see Fig. 2.4). Deep etching leads to an effective parabolic potential that confines the electrons in a much smaller region than the metallurgical diameter of the pillars. In addition it removes all possible luminescence signals from the QW that could interfere with the inelastic light scattering signal. An example of the QDs fabricated during this thesis work is shown in Fig. 3.4.

3.1.3 Surface states in GaAs QDs

The carrier distribution close to the lateral surface suffers dramatic modifications induced by the etching process. Toward the boundary of the QD, were the semiconductor is in contact with air, carrier depletion occurs as a result of surface states. These surface states are caused by the incomplete covalent bonds (dangling bonds) at the surface of the semiconductor. They result in electron energy levels within the energy band-gap. Surface states cause the pinning of the Fermi level. This leads to a natural surface depletion and a mismatch of the bottom of the conduction band between the edge and bulk regions of the semiconductor that for GaAs is of about 0.6 eV.

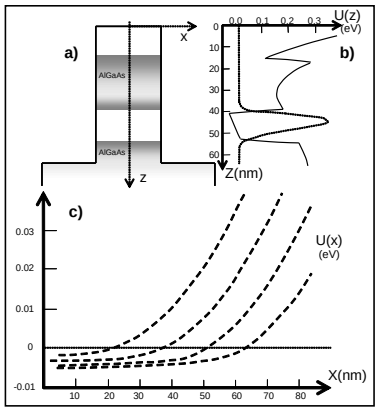

FIGURE 3.5: a) Schematic representation of a vertical quantum dot. b) Calculated band profile $U(z)$ along the growth direction (solid line) and electron density (dotted line). c) Calculated effective confining potential along one of the radial directions of the pillar in the GaAs QW region. The parameters used for the calculations are a pinning of the Fermi level at the edge of ϕ=0.6 eV, QW width of z=43 nm and pillar radius from left to right of D=300, 320, 340 and 360 nm. The cap and donor layers were doped with a density of ρ=10^{18}donors cm^{-1}, similarly to the QW structures used in this work for the fabrication of single QDs. Data after reference [57].

In an ordinary three dimensional homogeneous material in contact with air, the depletion width can be obtained by solving the Poisson equation within the depletion approximation [56]. The width of the depletion layer w calculated in this way is:

$$w \sim \left[\frac{1}{n}\frac{2\epsilon\phi}{e}\right]^{1/2} , \tag{3.2}$$

where n is the free carrier density, ϵ is the dielectric constant of the material and e the electron charge. ϕ is the band offset due to the pinning of the Fermi level estimated to be close to $\phi \sim 0.6$ eV below the conduction band in the GaAs, although this number may change depending on the etching process due to the introduction of additional defects. It is important to note that the depletion region is inversely proportional to the square root of the electron density.

In modulation-doped QWs complications arise from the 2D nature of the confinement region and fro the presence of the δ-doping layers. The depletion layer in this case can only be obtained by solving a self-consistent three-dimensional Poisson-Schrödinger equation with the 2D nature of the free electrons properly taken into account. Since the thickness of the QWs is typically only several tens of angstroms, the electric field in the vicinity of these regions can be highly distorted compared to the bulk case. Additional quantum effects in QDs due to the

QD confinement that modify the electronic structure must be taken into account.

In doped GaAs nano-structures similar to the ones of our QDs [58, 59] several experimental groups reported depletion regions ranging from 500 nm to 60 nm. This large variety of results can be attributed to the introduction of additional defects during the etching process in the surface exposed to air. Depletion widths of ≈90 nm will be reported in this thesis work from QD's fabricated on samples with densities around 10^{11}cm^{-2}.

To get further insights on these effects, Fig. 3.5 reports calculations of the effective confining potential along the radial direction of a GaAs nanostructure similar to those studied here [57]. In particular the results in panel (c) refer to a QW region of the pillar that has a structure along the growth direction similar to that of the samples studied in this thesis, and for several QD radius. The origin of the energy scale indicates the Fermi level, and its intersection with the potential profiles (dashed lines) determines the beginning of the depleted region. The calculated depletion lengths are consistent with those found in the experiments cited above.

When the dimensions of the dots are sufficiently small the depletion effects lead to a potential that can be well approximated to be parabolic. Strictly speaking the parabolic approximation can only be applied in the case of vanishing electron density because the screening effects of the confined electrons flatten the bottom of the parabola yielding an almost constant inner zone. In experiments with few electrons, the occurrence of a parabolic confinement potential is suggested by the absorption experiments that display only one peak due to a dipole transition. This verifies the Kohn theorem (see section 2.2.1) that holds in the parabolic potential approximation.

The number or electrons, the parabolic potential and the total density measured in the QW are parameters that depend on each other. In the approximation of parabolic potential and constant density the confinement energy is given by [1]:

$$\omega_0^2 = \frac{e^2}{4\pi\epsilon m^* r_s^3 \sqrt{N_e}} \ , \tag{3.3}$$

where r_s is the density parameter defined in section 1.2.

3.2 Experimental set-up for inelastic light scattering

The experimental set-up used for the spectroscopic investigation of electronic excitations in QD's requires very demanding characteristics in terms of tunability of the excitation laser energy, stray-light rejection, spectral resolution and signal-to-noise ratio. In the following the set-ups used in this work will be presented.

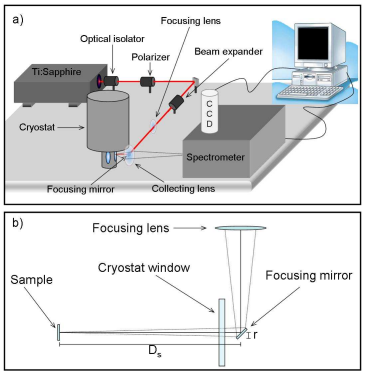

FIGURE 3.6: a) Schematic configuration of the set-up for inelastic light scattering experiments. The polarization of the exciting light from a ring-etalon cavity Ti-sapphire or dye laser is determined by a double Fresnel prism rotator. The laser beam is controlled by an optical filter that acts also as a beam expander and focused onto the sample placed into a cryostat. The scattered light is collected by a lens and focused in a double or triple grating spectrometer where the gratings act as polarizers. The signal is then collected by a multichannel detector. b) Details of the laser beam path between the focusing lens and the sample.

3.2.1 Optical set-up

Figure 3.6 (a) shows the scheme of the optical set-up used for the resonant inelastic light scattering experiments. Two types of lasers were used: Ti-sapphire and dye ring etalon lasers. Both offered a tunability between 770 nm and 870 nm, the spectral region of the QD interband resonances, and sharp lines with full width at half maximum < 5 MHz (around 20 neV).

The light is focused onto the sample with the smallest spot given the very long working distances imposed by the windows of the cryostat and by the arrangement of the optics necessary to collect the signal and to control the polarization. The minimum spot size can be calculated using the Airy formula used for gaussian beams:

$$S = 0.62\frac{\lambda \cdot r}{D_s} \ , \tag{3.4}$$

where S is the diameter of the spot of the laser at the beam waist, λ is the laser wavelength, r is the radius of the laser and D_s is the distance to the sample (see figure 3.6 (b)). In the case of experiments with the dilution cryostat the distance from the focusing mirror to the sample was around 40 cm while the beam radius at that distance was only a few mm. The laser spot on the sample surface achievable in this case ranged between 100 and 200 μm. Similar values were obtained for the experiments with the ^{4}He cryostat. The polarization control of

the exciting light was achieved by a double Fresnel prism polarization rotator and a linear polarizer. The backscattering configuration displayed in Fig. 3.6(a) was chosen in order to minimize the collection of the reflected light from the windows of the optical cryostats (not shown in Fig. 3.6).

Transfer of in-plane momentum to the electron system was achieved by tilting the sample at finite incidence angles. In the backscattering geometry, the in-plane component of the incident/scattered wave-vector of light inside the sample is the same as the in-plane component outside the sample, so the transferred wave-vector from the photon field is:

$$q = \frac{4\pi}{\lambda} sin(\theta) \tag{3.5}$$

where θ is the incident angle. The transferred wave-vector in the z direction, instead, is enhanced by the sample refractive index n, and is given by $\frac{4\pi n}{\lambda} cos(\theta)$. The intensity of the inelastically back-scattered light is increased by this effect. This intensity is, indeed, zero in the dipole approximation, when the oscillating electromagnetic fields are considered constant along the z direction, but becomes finite as the transferred wave-vector along z increases (see Eq. 2.12).

In the experimental conditions of backscattering described above, an indetermination in the angle is introduced by the solid angle of the optical cryostats ($\Delta\theta \approx 10^o$).

The scattered light was collected into a double or a triple Czerny-Turner spectrometer operating in additive mode using one or two collecting lenses in the case of experiments without and with magnetic field, respectively. In both cases the lenses were chosen taking into account the optical aperture of the spectrometer ($f/7.5$) in order to maximize both the resolution achieved and the signal collection. The spectrometers were equipped with master gratings with 1800 grooves/mm. A multichannel detector based on a liquid nitrogen cooled CCD camera was used. The spectral resolution using a 30 μm slit was below 20 μeV. The polarization of the detected scattered light was fixed by the spectrometer gratings.

In the final setup the laser beam passed first through an optical isolator to avoid any feedback to the laser. Then a polarization rotator followed by a linear polarizer was used. The intensity of the laser was tuned using neutral density optical filters. Then an optical filter was used to improve the laser quality and to control the diameter of the laser at the beam waist before the focusing lens. One of the most important requirements of these inelastic light scattering experiments is to avoid reflections of the laser from the windows. This was achieved by blocking the specular reflections with the focusing mirror and the other reflections with small black flags (made of optically absorbing tape) placed just before the collecting lenses.

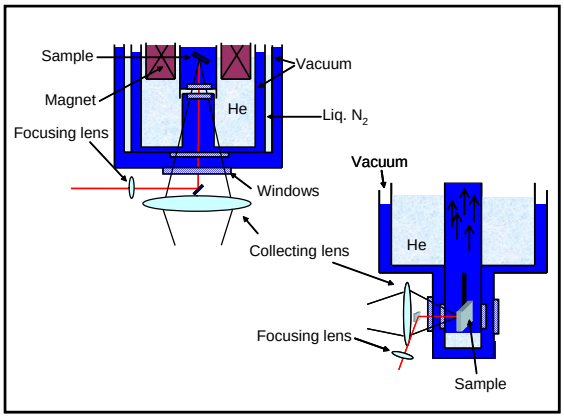

FIGURE 3.7: Schematic configuration of the optical setup close to the cryostats. Left cartoon: dilution cryostat; right cartoon: He-bath cryostat.

3.2.2 ^{4}He experiments

The experiments at zero magnetic field were carried out in a ^{4}He bath cryostat (Oxford Optistat) able to reach temperatures down to 1.5 K. The f number of the cryostat is 2.2 and the thermal isolation of the sample is achieved through two optical windows. In this cryostat the sample was placed 12 cm far from the external window and the imaging of the sample was achieved using a 5X objective and an infrared CCD at a working distance of approximately 15 cm. The illumination of the sample in the cryostat in order to identify the QD array was obtained using a white source coming from behind the infrared CCD.

3.2.3 Dilution cryostat and magnetic field

Experiments with magnetic fields were carried out in two dilution Oxford cryostats, Kelvinox 400 (Scuola Normale Superiore, Pisa, Italy) and Kelvinox 100 (Lucent Technologies, Murray Hill, NJ, USA) with cooling powers of 400 and 100 μW, respectively, and with available magnetic fields up to 16 T. These cryostats reach temperatures down to 45mK. Thermal isolation of the sample is achieved in both cases through four optical windows made of Spectrosil B, which transmits the light in the range of interest around 800nm and blocks the electromagnetic radiation below 4 μm. This configuration allows to excite the samples with laser and collect the scattered light as explained in the paragraphs above. The f number of the cryostats is 3.6. Samples are placed at the end of a copper rod located 24 cm far from the room temperature window and attached

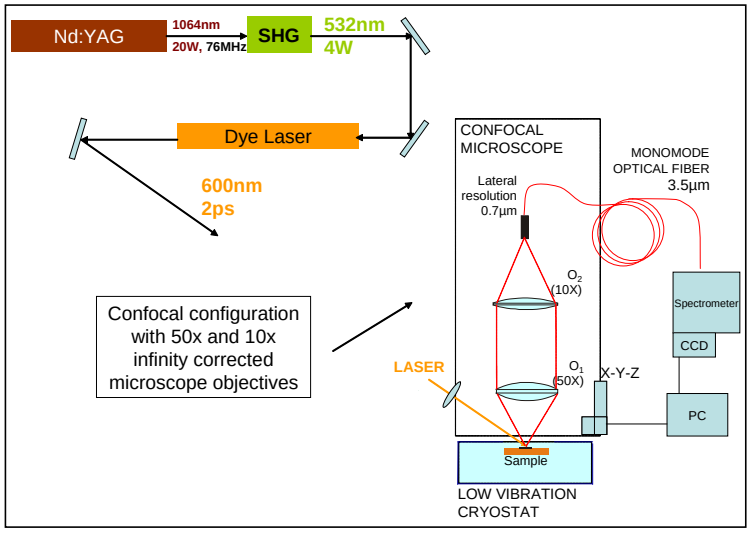

FIGURE 3.8: Schematic configuration of the optical set-up used for micro-luminescence experiments. The laser light was produced by a pulsed Nd-YAG laser system and then focused onto a wide area of the sample placed in a low vibration cryostat. The light collected by a confocal microscope allowed a lateral resolution of 0.7μm.

to the mixing chamber of the dilution refrigerator. Illumination for imaging was achieved defocusing the laser onto the sample. Optical imaging is achieved using a CCD placed at one of the focus planes of the first collecting lens.

Figure 3.7 shows a schematic representation of the optical setups and cryostats.

3.2.4 Micro-luminescence (μ-PL) experiments

For the μ-PL experiments, a dye laser pumped by the second harmonic of a Nd:YAG pulsed laser was used as the excitation source. The excitation wavelength was 600 nm and the duration of the pulse was 2 ps with a repetition rate of 76 MHz. For the collection, a confocal configuration of two infinity corrected microscope objectives was used. The PL signal was then focused into a monomode optical fiber with a core diameter of 3.5 μm assuring a lateral resolution of 0.7μm (see Fig. 3.8). A single grating spectrometer and a CCD camera were used for the detection. All μ-PL experiments reported here were carried at 5.7 K in a low-vibrational cryostat.

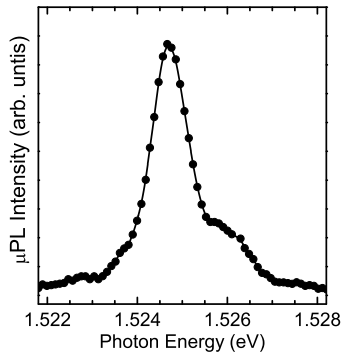

FIGURE 3.9: μ-PL spectrum of a single dry-etched QD of geometrical diameter D = 280 nm at T = 5.7 K. The power density is 5×10^{-3} W/cm^2.

3.3 Luminescence from GaAs/AlGaAs nano-fabricated quantum dots

Single-dot μ-PL of the nano-fabricated GaAs/AlGaAs QDs will be presented in this section. The samples were fabricated as described in the previous sections of this chapter. It will be shown below that this spectroscopic analysis allows to gain insights on QD confinement and to prove the uniformity achieved in the fabrication of the dilute arrays of QDs.

Figure 3.9 shows the low temperature μ-PL spectrum of one of the single dry-etched QDs of geometrical diameter D = 280 nm shown in the scanning electron microscope pictures of Fig. 3.10. This sample is composed by an array of QDs with dimensions 100×100 μm with a dot to dot separation of 1 μm. However the data presented in this section were taken with a confocal set-up achieving a lateral resolution of 0.7μm and able to detect the PL from single QDs. The power density used in the spectrum showed in Fig. 3.9 is 5×10^{-3}W/cm^2.

The peak at $\approx$ 1525 meV is assigned to the QD PL and it is blue shifted from the QW peak as shown in Fig. 3.10. The small higher energy shoulder seen in Fig. 3.9 is observed at the same energy position in other QD arrays with different diameters and it is assigned to recombination from the Si-doped AlGaAs layer, probably linked to deep donor acceptor pairs [1].

[1]This high-energy shoulder is not observed outside of the QD array where the sample is etched beyond the doping layer and in the QW. In addition, the peak is not seen with excitation photon energy below the AlGaAs band-gap. As expected for recombination from deep donor-acceptor pairs, the peak is blue shifted at high power density [60].

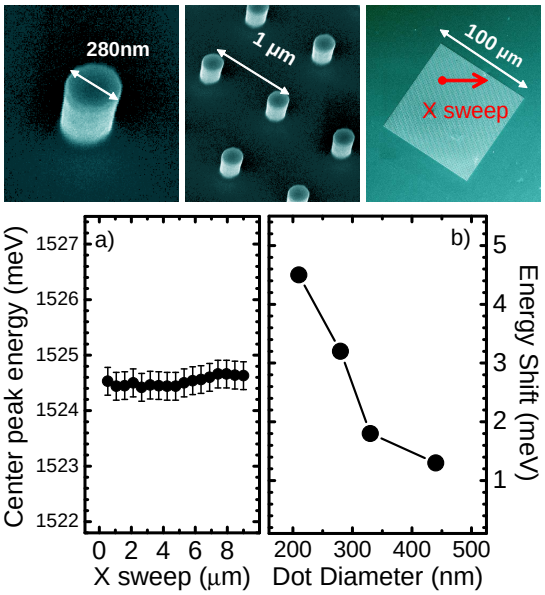

FIGURE 3.10: a) Dispersion of the peak energy of the spatially resolved μ-PL along the direction shown by the red arrow in the SEM picture. b) Energy shift of the QD peak from the quantum well emission for different QD diameters.

The homogeneity of the optical emission of the QDs was inferred by performing spatially-resolved PL experiments along the arrays that revealed identical spectra from different excited QDs leading to a macro-PL very similar to the μ-PL spectrum. Figure 3.10 (a) shows the evolution of the μ-PL peak energy along the direction set by the red arrow in the SEM pictures. These data demonstrate that along 9μm the luminescence peak does not change its emission energy within the experimental errors.

The evolution of the energy shifts of the QD peaks from the QW emission ranges from 1 meV for the D = 440 nm QD up to 4.6 meV for the D = 210 nm QD (Fig. 3.10(b)). These large energy shifts offer a first estimation of the confinement energy for different QD dimensions [61].

Finally the QD emissions can be well described by Lorentzian line-shapes suggesting homogeneous broadening as expected for single-dot luminescence. However, full widths at half maximum (FWHM) of the emission peaks are much larger than those usually observed in single-dot PL with a value of 0.7 meV for the QDs with D = 280 nm. The FWHM increases for larger dots and becomes 2.7 meV for D = 330 nm. These facts suggest that the wide emission lines observed

could be linked to the built in electron population that creates fast relaxation channels for the photoexcited electron-hole pairs (see reference [62]).

In conclusion, the data presented in this chapter prove the presence of a confinement potential in the nano-fabricated GaAs/AlGaAs QDs with a limited and controlled number of electrons and very high homogeneity of the QD properties within the array.

Chapter

4 Quantum dots with many electrons

This chapter focuses on the excitation spectra of electrons confined in semiconductor QDs in the regime of large electron population. In this limit the electron occupation of several Fock-Darwin shells gives rise to a rich excitation spectrum composed by equally-spaced peaks associated to consecutive inter-shell modes. The spectra presented in this chapter offer direct evidence of the shell structure of the QD and allow to estimate the confinement energies and the number of occupied shells.

The last part of this chapter is devoted to coupled QDs. It will be shown that the interplay between the tunneling gap and the confinement energy leads to new excitations in the resonant light scattering spectra.

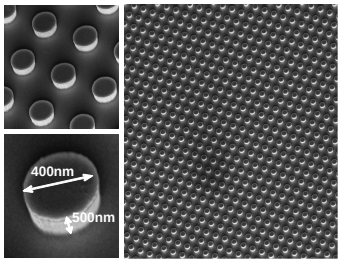

FIGURE 4.1: Scanning electron microscope pictures of 100 × 100 μm arrays of QDs with lateral diameter D = 400 nm. The separation between QDs is 1 μm.

4.1 Inelastic light scattering spectroscopy of Fock Darwin states in quantum dots

The experimental framework of QDs introduced in chapter 2 focused on the shell structure and spin-filling in QDs, which have been extensively studied by magneto-transport methods [15]. In these experiments QD states are accessed by coupling the QDs with source and drain metallic leads and by studying the tunneling of electrons in and out of the QDs. On the contrary, the inelastic light scattering methods used here offer direct signatures of neutral excitations under experimental conditions in which the total charge in the QD remains unchanged.

This section presents resonant inelastic light scattering experiments from nano-fabricated AlGaAs/GaAs QDs with lateral diameter D = 400 nm. Owing to their large geometrical dimensions the dots studied in this chapter are populated with a high number of electrons (N_e), which results in the occupation of several Fock-Darwin shells. The light scattering spectra from these dots are characterized by a sequence of equally spaced peaks that correspond to excitations that are interpreted as transitions between consecutive Fock-Darwin shell states with the same parity.

Samples were fabricated as described in sections 3.1.1 and 3.1.2. Figure 4.1 shows scanning electron microscope images of the QDs. One of the features to be noted is the very high homogeneity in the size distribution of the QDs in the array as also pointed out by the μ-PL analysis discussed in section 3.3. It must be stressed that electrons trapped in surface states lead to an electron depletion layer and to an effective confinement region with a diameter much smaller than the metallurgical size of the QD (see section 3.1.3). It will be shown in the following that the properties of the spectra here presented allow to estimate the confinement energy (i.e. the depletion width) and the effective number of confined electrons.

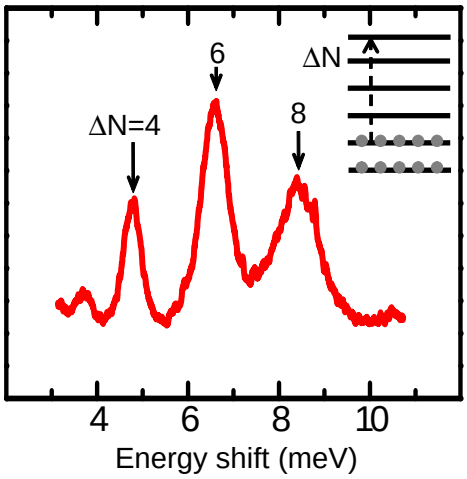

FIGURE 4.2: Low temperature (1.9 K) inelastic light scattering spectrum from D = 400 nm QD array in the backscattering configuration with parallel incident and scattered photon polarizations. The incident laser energy is 1561 meV. A representation of the $\Delta N = 4$ excitation between different Fock-Darwin shells with the same orbital symmetry is shown in the inset.

4.1.1 Inter-shell excitations

Figure 4.2 displays a representative low temperature (T = 1.9 K) resonant inelastic light scattering spectrum with parallel incoming and outgoing photon polarizations (polarized configuration) obtained from the D = 400 nm QD array described above. The spectrum is characterized by a set of low energy excitations that are regarded as a proof of the lateral confinement achieved in these pillars. The energies of these excitations are similar to the ones reported in previous experiments on dry etched GaAs QDs with similar metallurgical size [21]. The spectrum is interpreted using the Fock-Darwin model (section 1.1.3). The simplest backscattering inelastic light scattering experiment is a second order process that allows excitations between states with the same parity ($\Delta N = 2, 4, 6...$). Within a Fock-Darwin framework these excitations are equally spaced, with an energy separation given by twice the effective confinement energy $\hbar\omega_0$ of the doped QDs. Following the parity selection rule and the energy position, the equally spaced excitations at 4.5, 6.4 and 8.4 meV are interpreted as inter-shell excitations between consecutive shells with same parity. The separation between these excitations corresponds to $2\hbar\omega_0$ (on average ~ 1.9 meV). An additional peak can be seen close to 3.7 meV which is separated from the $\Delta N = 4$ peak by only one unit of $\hbar\omega_0$. This peak will be further discussed in this section.

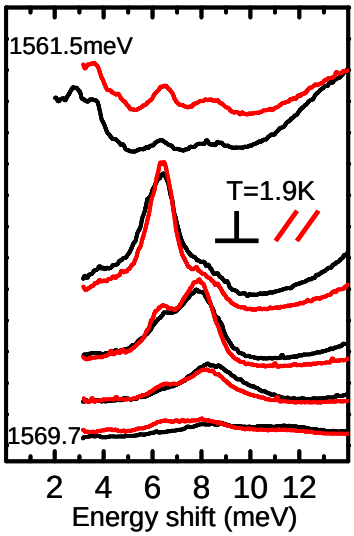

FIGURE 4.3: Low temperature (T = 1.9 K) resonant inelastic light scattering spectra of the QD sample with D = 400 nm in the backscattering configuration. Incident laser energies range from 1561.5 to 1569.7 meV from top to bottom. Polarized and depolarized signals are depicted in red and black colors, respectively.

Figure 4.3 displays the spectra at different incident laser energies. Polarized and depolarized configurations are shown in red and black colors, respectively. Up to five peaks can be seen within the explored resonance in backscattering configuration. These peaks have a constant energy shift with respect to the laser energy as expected from inelastic light scattering excitations. Additionally, these modes display no energy shift between the two polarization configurations.

Previous theoretical [50] and experimental inelastic light scattering studies [20, 21, 22, 63] of QDs containing few hundreds of electrons reported a similar behavior under strong resonance conditions. These resulsts and the absence of splitting between the peaks in the two polarization configurations (shown in Fig. 4.3) allow to refine the interpretation of the data in Fig. 4.2 based on the Fock-Darwin model. Indeed the peaks in perpendicular and parallel polarizations reported in Fig. 4.3 can be ascribed to spin and single particle modes respectively. As explained in chapter 2 the spin excitations are usually red-shifted from the single particle modes by Hartree and exchange-correlation dynamical corrections. The absence of energy splitting between the two excitations is attributed to a cancellation of the exchange-correlation terms that occurs when many energy levels are populated [21]. This is also confirmed by the calcula-

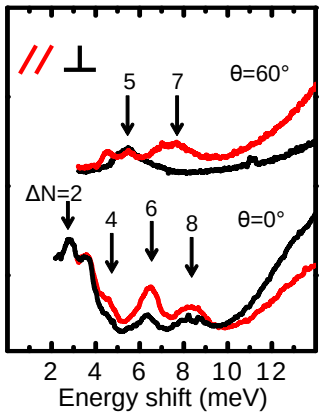

FIGURE 4.4: Polarized (red) and depolarized (black) resonant inelastic light scattering spectra of QDs with D = 400 nm in the backscattering configuration ($\theta = 0^o$) and at finite incident angle ($\theta = 60^o$). The spectra are taken at the laser photon energy of 1561.5 meV and at T=1.9 K.

tions reported in Ref. [50] (also shown in Fig. 2.8) of the oscillator strength of the $\Delta N = 2$, $\Delta M = 0$ monopole spin and single particle modes for different electron occupation. Finally, it should be remarked that additional excitations corresponding to the collective plasmon inter-shell modes should occur in the high-energy part of the spectrum due to the expected large impact of depolarization effects. However these excitations have not been detected within the studied range of laser wavelengths probably because of the impact of the luminescence signal at high energy and of the overlap with the single particle modes with large ΔN.

Intershell excitations at finite incident angle

Selection rules dictate that monopole excitations ($\Delta M = 0$) dominate the Raman spectra at zero incident angle. At finite incidence angle θ (see cartoon in Fig. 2.6) new modes with $\Delta M \neq 0$ become active due to the transfer of in-plane wave-vector in the light scattering process. Experimentally, the in-plane wave-vector is transferred to the system in the backscattering geometry by tilting the sample with respect to the direction of the incident light.

Figure 4.4 shows the inelastic light scattering spectra at T=1.9K and at the laser excitation energy of 1561.5 meV. Figure 4.4 shows the spectrum in the backscattering configuration at $\theta = 0^o \pm 9^o$ ($\Delta q \approx 0 \pm 2.5 \times 10^4 cm^{-1}$) and the spectrum at $\theta = 60^o \pm 9^o$ ($\Delta q \approx (1.3 \pm 0.1) \times 10^5 cm^{-1}$). At $\theta = 60^o$ two additional peaks (labeled $\Delta N = 5$ and $\Delta N = 7$) are seen at energies of $\approx$ 5.4 meV and

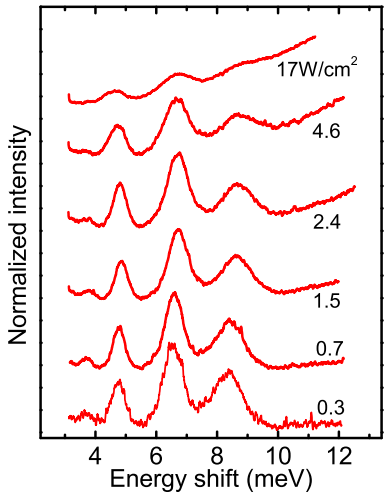

FIGURE 4.5: Power dependence of the inelastic light scattering spectra from QDs with D = 400 nm. Spectra were taken using the parallel polarization configuration at a laser energy of 1561 meV and at a temperature of 1.9 K. The incident laser intensity ranges from 0.3 W/cm^2 to 17 W/cm^2.

$\approx$ 7.4 meV and assigned to dipole excitations with $\Delta M = \pm 1$ and odd integer change of ΔN. These two peaks together with the ones already detected at zero incidence angle lead to equally-spaced modes which are identified with single particle excitations associated to integer changes of ΔN. This behavior confirms the origin of the excitations as monopole and dipole electronic excitations among consecutive Fock-Darwin states separated by $\hbar\omega_0 = 1 \pm 0.1$ meV. At zero angle, possible small asymmetries or residual disorder in the QD parabolic confinement can also break the parity selection rules. An example is given by the $\Delta N = 3$ mode that is observed in the backscattering geometry.

In summary, inelastic light scattering spectra offered evidence of a shell structure in QDs populated by many electrons. The absence of splittings between the polarized and depolarized configurations is attributed to the cancellation of the many body contributions and it allows to describe the excitation spectra within a Fock-Darwin framework.

Power and temperature dependence

Two effects should be taken into account as the intensity of the excitation laser increases: (1) photo-generation of electron-hole pairs that can increase the ef-

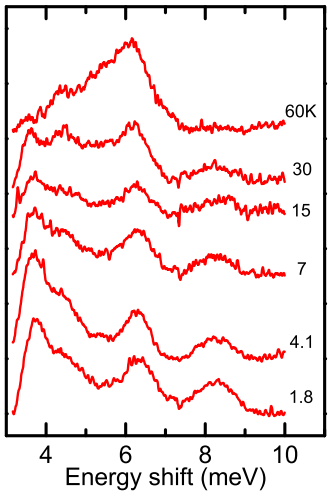

FIGURE 4.6: Temperature behavior of polarized inelastic light scattering spectra in QDs with D = 400 nm. The spectra are presented after subtraction of the background and taken at a laser energy of 1561 meV and excitation intensity of 1.5 W/cm^2. The temperature ranges from 1.8 K to 60 K.

fective QD electron population in the conduction band and (2) local increase of temperature. The first effect becomes relevant when the inter-band relaxation time is larger than the time required to optically generate each pair. Figure 4.5 shows the polarized inelastic light scattering signal as a function of the excitation intensity at a temperature of 1.9 K. The spectra in Fig. 4.5 do not manifest any appreciable change in their shape other than an increase of the background, indicating that the relative change in the electron population is not enough to modify the excitation spectrum. This is consistent with the fact that the QDs are already populated by many electrons. This behavior is in sharp contrast to what found in the few-electron regime that will be presented in the following chapter.

In order to rule out a possible effect due to the local increase of temperature Fig 4.6 reports inelastic light scattering spectra at different temperatures. The excitations seen at T = 1.9 K remain up to temperatures of 60 K. The change in the relative intensities of the excitations could be simply linked to electron redistribution among the different shells that occurs due to thermal excitation of electrons.

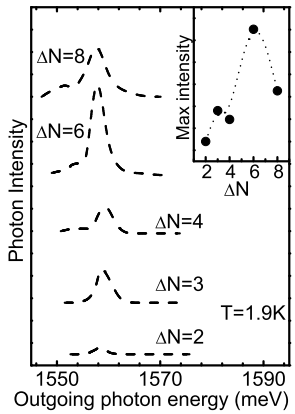

FIGURE 4.7: Enhancement profiles of the inter-shell modes in the D = 400 nm QDs. The inelastic light scattering peak intensities are plotted as a function of $E = E_{in} - E_{\Delta N}$ where E_{in} is the incident laser energy and $E_{\Delta N}$ is the energy of the corresponding inter-shell excitation. Inset: maximum value of the enhancement of light scattering intensities at resonance plotted as a function of ΔN.

4.1.2 Inter-band properties

The cross section of the inelastic light scattering intensity incorporates a resonant denominator linked to electron-hole excitations across the band-gap of the material (see Eq. 2.9). For this reason, the intensities of individual QD electronic excitations seen in light scattering depend on the incident laser energy and display a resonance enhancement profile as demonstrated in Fig. 4.7. Figure 4.7 reports the light scattering peak intensity as a function of E where $E = E_{in} - E_{\Delta N}$, E_{in} is the incident laser energy and $E_{\Delta N}$ is the energy of the inter-shell transition associated to a given ΔN. When plotted in these relative energy units, the resonance profiles show a single narrow peak (with FWHM of 2 meV) at around 1558 meV. These results demonstrate the strong outgoing resonance conditions exploited in the experiments here presented.

Number of electrons

The results shown in Fig 4.7 offer a way to estimate the effective confinement radius, and therefore the effective number of confined electrons. To this end it should be noted that the intensity of the Raman cross section for individual ΔN transitions results from the competition between two effects. One is related to the magnitude of the matrix elements that is expected to decrease with increasing ΔN. The other is given by the number of states that contribute to the transition

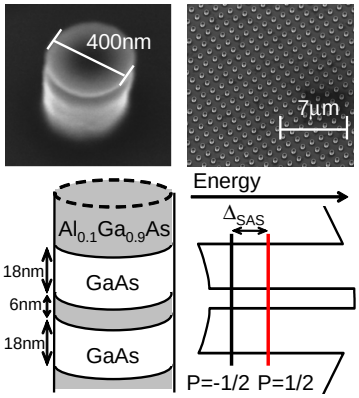

FIGURE 4.8: Top: SEM images of one dry-etched coupled quantum dot (QDs) and the $100\mu m$ x $100\mu m$ array composed by 10^4 coupled QDs separated by $1\mu m$. Bottom: Schematic description of the vertical double QD and the corresponding energy diagram in the conduction band along the growth direction. The two lowest symmetric and antisymmetric levels are also shown. P is the pseudo-spin, Δ_{SAS} is the tunneling gap of the coupled QD.

that increases with ΔN. In the inset to Fig 4.7, the maxima of the resonant enhancement of the light scattering intensities are plotted for different values of ΔN. The maximum intensity of the ΔN modes should thus occur when ΔN coincides with the last occupied shell N (which gives the largest number of contributing states).

Equation 1.25 can then be used to find the link between the effective dimensions of the dot and the number of electrons. If N now defines the number of occupied shells, the depletion width ξ is given by:

$$\xi = R - \sqrt{N \cdot \langle \rho^2 \rangle_{N=1}} \ , \tag{4.1}$$

where R is the metallurgical radius of the dot. Considering that the maximum inelastic light scattering intensity occurs for modes with ΔN between 6 and 7 (which yields a number of electrons between 42 and 56), the depletion width is estimated to be $\xi = 100$ nm. This depletion width is consistent with calculations and experimental results discussed in section 3.1.3.

4.2 Double quantum dots

It has been shown in the previous section that the inelastic light scattering spectra in QDs with many electrons can be interpreted in terms of single particle inter-

shell transitions within a Fock-Darwin framework. This framework is also used here to interpret tunneling excitations of electrons in dry-etched modulation-doped vertical AlGaAs/GaAs coupled quantum dots (QDs) in the regime of many-electron population.

Coupled QDs are of particular relevance for quantum computation schemes [9, 10]. In fact, as explained in chapter 1, the tunneling between the two QD states modulates the exchange interaction and provides a route toward entanglement of two spins [11]. Additionally, the electron states in coupled double QD are expected to be less sensitive to dephasing mechanisms linked to coupling of spin and charge states to the environment such as the coupling to nuclear spins. Coupled QDs also offer ways to study novel spin and charge collective phases and quantum phase transitions at the nano-scale [33].

Several experimental studies have shown the remarkable physics and possible applications of coupled QDs. Transport experiments have extensively investigated inter-dot coupling effects in the strong and weak coupling regimes [43, 64, 65]. These measurements have provided evidence for the impact of symmetric and anti-symmetric states in the Coulomb blockade spectra and have demonstrated slower relaxation rates for spin states in laterally coupled QDs and their coherent manipulation. Inter-band luminescence experiments have also been carried out in self-assembled InAs coupled QDs [66] showing anti-crossing of the luminescence lines due to inter-dot coupling.

This section reports the observation of low-lying neutral excitations of electrons in vertically-coupled GaAs / AlGaAs double QDs nano-fabricated by e-beam lithography and dry etching. A sequence of intra- and inter-shell excitations are found at energies determined by the interplay between the QD confinement energy $\hbar\omega_o$ and the tunneling gap Δ_{SAS}, the splitting between the symmetric and anti-symmetric delocalized single particle states. The spectra reveal sharp excitations, with FWHM below $200\mu eV$, that demonstrate the high quality of these etched nano-structures. The narrow line-widths displayed by the electronic excitations in these nano-structures indicate promising venues for the spectroscopic investigation of entanglement of electron states in these QDs.

4.2.1 Determination of the confinement energy and tunneling gap

Coupling between the two dots leads to the splitting of the Fock-Darwin single dot levels in bonding (symmetric) and anti-bonding (antisymmetric) levels separated by the tunneling gap Δ_{SAS}. The single particle eigen-energies of parabolic double QDs at zero magnetic field can be modeled by Eq. 1.31.

The top panels in Fig 4.8 show scanning electron microscope (SEM) images of the coupled QDs. The value of the lateral diameter was chosen in order to

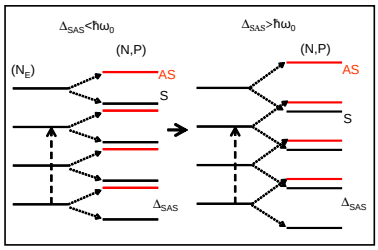

FIGURE 4.9: Schematic representation of QD coupling in the case of $\Delta_{SAS} < \hbar\omega_0$ (left) and $\Delta_{SAS} > \hbar\omega_0$ (right).

yield a confinement energy similar to the QDs studied in the previous section and comparable with the magnitude of the tunneling gap. Owing to the large dimensions and to the higher doping of the substrate these QDs are expected to have a large number of electrons.

The peculiar energy-level structure of double quantum dots yields an excitation spectrum characterized by tunneling or pseudo-spin modes with $\Delta P = \pm 1$ constructed from intra- or inter-shell excitations of electrons from the symmetric to the anti-symmetric QD levels. Figure 4.9 shows the FD sequence following Eq. 1.31 for the cases $\Delta_{SAS} < \hbar\omega_0$ and $\Delta_{SAS} > \hbar\omega_0$ that reveals the richness of the energy level structure determined by the interplay between Δ_{SAS} and $\hbar\omega_0$.

As seen in previous chapters, parity selection rules now applied to parabolic double coupled QDs establish that monopole transitions with $\Delta m = 0$ ($\Delta N = 0, 2, 4, \ldots$) and $\Delta P = 0, \pm 1$ are the strongest intensity modes active in light scattering experiments in a backscattering geometry [20, 21, 22, 53]. The single-particle representations of intra- and inter-shell pseudo-spin excitations associated with changes of N and P are shown in Fig. 4.10 as vertical arrows.

Light scattering experiments were performed in a backscattering configuration ($q \leq 2 \times 10^4$ cm^{-1} where q is the wave-vector transferred into the lateral dimension) with temperatures down to $T = 1.9$ K.

Figure 4.10 shows the resonant inelastic light scattering spectra at different excitation energies and T=1.9 K after conventional subtraction of the background due to inter-band luminescence and laser tail. The laser was tuned between 1528.6 meV (bottom spectrum) to 1534.5 meV (top spectrum) to explore different resonances. The spectra were taken in a depolarized configuration with perpendicular polarizations of the incoming and outgoing light in order to reduce the stray laser light and with a laser intensity of 0.1 W/cm^2 [67].

Spectra shown in Fig. 4.10 are remarkably different from those found in single QDs with the same lateral diameter and discussed in the previous section. In single QDs the resonant inelastic light scattering spectra display a sequence of

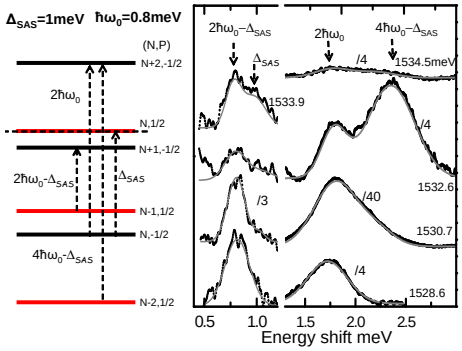

FIGURE 4.10: Left: schematic representation of energy levels and transitions in coupled QDs. N and P are the shell and pseudo-spin quantum numbers, respectively. Black and red lines represent symmetric and antisymmetric levels, respectively. The dotted line marks the position of the Fermi level that accounts for the observed reduced intensities of the two lowest-energy modes. Right panel: Resonant inelastic light scattering spectra at 1.9K and at different laser energies (shown in the figure) in depolarized configuration. Intensities were scaled by factors indicated in the figure.

peaks equally spaced in energy by $2\hbar\omega_0$ with a FWHM of 1 meV in agreement with data obtained by other groups [21, 20, 22]. The spectra of double QDs are instead characterized by two sharp (FWHM = 0.2 meV) low-energy peaks that are assigned to excitations at $2\hbar\omega_0 - \Delta_{SAS}$ and Δ_{SAS}. The peak at 1.8 meV corresponding to $2\hbar\omega_0$ is thus assigned to the conventional inter-shell ΔN=2 mode also observed in single QDs. The peculiar energy level structure of the coupled QDs is additionally revealed by the fourth highest-energy peak shown in Fig. 4.10 and observed at an energy corresponding to $4\hbar\omega_0 - \Delta_{SAS} = 2.4$ meV. The energy of this peak shifts from 2.2 to 2.6 meV depending on the laser excitation wavelength. This behavior can be linked to non-parabolicity effects whose impact increases with the energy of the mode and to partial overlap with the $2\hbar\omega_0 + \Delta_{SAS}$ inter-shell pseudo-spin mode expected at ~2.8 meV. More broad excitations were detected at higher energies (data not shown) with decreasing intensity corresponding to higher inter-shell excitations. It can be noted that the energy of the intra-shell pseudo-spin mode ($\Delta_{SAS} \sim 1$ meV) is higher than the value of the tunneling gap measured in the double quantum well prior to nano-fabrication (~ 0.8 meV). This could be linked to partial depletion of electrons caused by the etching processes.

The difference in the intensities between the modes below 1 meV and those at higher energies is remarkable. It suggests partial population of the two highest-energy occupied levels as indicated by the position of the Fermi level shown by the dotted line in the left part of Fig. 4.10. These two levels are the excited states

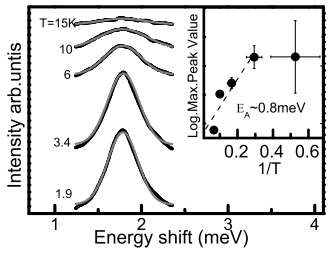

FIGURE 4.11: Temperature dependence of the monopole inter-shell transition at $2\hbar\omega_o$. Laser intensity and energy are 0.1 W/cm^2 and 1567 meV, respectively. Spectra are presented after conventional subtraction of background due to luminescence and laser tail. The inset shows an Arrhenius plot of the integrated intensity with an activation energy of 0.8 meV.

associated with the two sharp low-lying transitions. Their partial population explains the reduced intensities of the two modes due to phase space filling effects. The results in Fig. 4.10 therefore suggests that light scattering can be applied to determine both energies and population of molecular states in coupled QDs.

Further evidence of the impact of inter-dot coupling arises from the temperature behavior of the conventional intra-shell monopole excitation at $2\hbar\omega_0$. Contrary to the single QD case, in fact, where this excitation remains unchanged up to temperatures above 30K, here a significant change of the signal intensity occurs at much lower temperatures and the inter-shell mode disappears at around 15 K with an activation energy of 0.8 meV as displayed in Fig 4.11. The activation gap is consistent with the value of $2\hbar\omega_0 - \Delta_{SAS}$, the gap separating the highest-energy occupied level (an antisymmetric state with shell number N) from the lowest-energy unoccupied level (a symmetric state with shell number $N + 2$). This behavior thus offers further evidence of the impact of inter-dot coupling in the excitation spectrum.

In conclusion the excitation spectra of nano-fabricated vertically-coupled quantum dots reveal a low-lying intra-shell pseudo-spin mode across the tunneling gap as well as inter-shell excitations resulting from the interplay between the confinement energy and the tunneling gap. The results presented here suggest that, by offering access to molecular-like excited states in the coupled QDs, the light scattering methods can provide a wealth of quantitative information on the energy level sequence, level occupation and tunneling gap in double QDs.

Chapter

5 Correlated states in quantum dots with few electrons

The study of highly correlated systems is at the heart of modern condensed matter science. The growing interest in zero dimensional states and experimental methods able of measuring the effects of electron interactions at the nano-scale is further stimulated by possible applications in areas such as quantum information and cryptography [9, 43, 11, 12]. As shown in the previous chapter, inelastic light scattering spectra from QDs that contain many electrons manifest the single-particle shell structure of the QD. These results are conceptually similar to the experiments of electrical transport in QDs, where Coulomb blockade peaks are usually interpreted in terms of charging energy and single particle Fock-Darwin states. In this chapter it will be shown that light scattering spectra in QDs with few electrons reveal interaction phenomena beyond the single-particle picture.

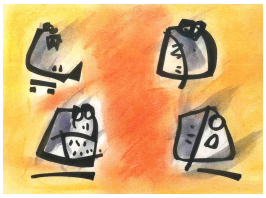

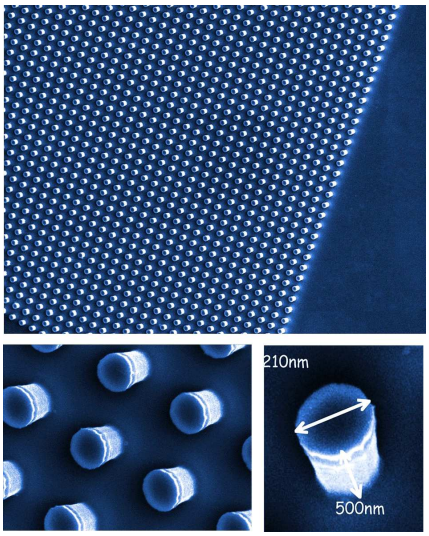

FIGURE 5.1: Scanning electron microscope pictures of fully processed quantum dots with D= 210 nm. Top view demonstrates the high homogeneity of the QDs within the array. The other panels display single QDs. The sequence of AlGaAs/GaAs layers can be seen as darker/brighter features at the edge of the QD.

5.1 Collective excitations in quantum dots with few electrons

Semiconductor QDs in the low-density regime are expected to display novel ground and excited states that manifest Coulomb interactions effects at the nano-scale [1]. These systems are also predicted to undergo quantum phase transitions as the strength of electron interactions is changed by some external parameters [5, 6]. In addition to their relevance for fundamental physics, few-electron QDs open the possibility to create quantum bits for quantum information processing. Transport in few-electron QDs coupled to metallic leads and excitonic optical recombination measurements have explored the impact of exchange energies and spin relaxation times in these nano-sized objects [68, 28, 14, 69, 70, 71, 72, 73, 74]. The remarkable transport experiments offered initial evidence for roles played by interactions that emerge as the number of electrons in the QD is changed.

The regime of few-electron occupation is expected to deeply affect the inelastic light scattering spectra. To this end it is useful to recall the theoretical data shown in Fig. 2.8 that report the evolution of single-particle modes and

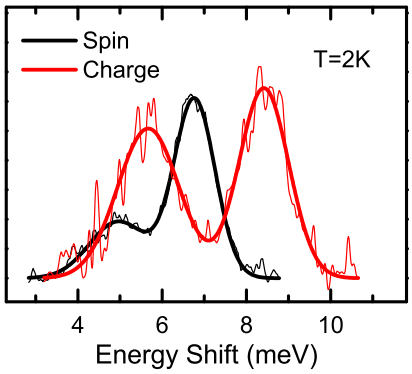

FIGURE 5.2: Low temperature (T = 2K) polarized (red) and depolarized (black) resonant inelastic light scattering spectra from QDs with a diameter D = 280 nm. The spectra were taken in the backscattering configuration at a laser energy of 1575.3 meV and 1570.5 meV for the polarized and the depolarized spectra, respectively. Background subtraction and fitting with two gaussian curves have been included for a better visual identification of the excitations. Due to polarization selection rules, the polarized and depolarized spectra are identified with charge and spin excitations, respectively.

spin excitations as the number of electrons is reduced. The observed shift of the spin excitations from the single-particle modes in the few-electron regime is linked to the impact of dynamical exchange-correlation energies that, as shown in chapter 4, is not visible in the regime of many shells occupied.

In order to detect the increasing importance of interaction effects predicted in the few electron regime, QDs were fabricated using the same 25nm wide, one-side modulation-doped $Al_{0.1}Ga_{0.9}As/GaAs$ quantum well already described in chapter 3. QD arrays with sizes $100\times100\ \mu$m containing 10^4 single QD replica, were defined by electron beam lithography with different diameters. This chapter focuses on QDs having lateral lithographically-defined diameters between 210 nm (shown in Fig. 5.1) and 280 nm for which the number of confined electrons is expected to be less than 10. The inelastic light scattering experiments in such QDs reveal a splitting of spin and charge inter-shell excitations, an effect that was not seen in QDs with larger dimensions and therefore with larger electron occupations.

Figure 5.2 displays representative polarized (red) and depolarized (black) resonant inelastic light scattering spectra from QDs with a nominal diameter of D = 280 nm in the backscattering configuration at T≈2 K. Background sub-

traction and fitting with two gaussians have been included for a better visual identification of the excitations. As argued in section 3.1.3 the depletion width in our samples is of the order of ≈ 100 nm. Under such conditions the presence of an electron population inside the QD potential created by etching and external depletion is not obvious. The inelastic light scattering signal presented in Fig. 5.2 demonstrates the presence of a finite electron population in these QDs.

The impact of the electron-electron interactions can be seen if one compares the spectra in Fig 5.2 with the ones from the QD's presented in the previous chapter. The latter spectra, shown in Fig. 4.3 in the case of QDs with D = 400 nm, displayed no splittings between polarized and depolarized modes. On the contrary, the excitations shown in Fig. 5.2 display a marked splitting between the polarized and depolarized spectra that signals that the few-electron regime is achieved.

Since the electron-electron interactions do not change the cylindrical symmetry of the system, collective QD states can still be classified in terms of the total angular momentum M and its z-component, the total spin S, and its z-component S_z. The selection rules in QDs applied to experiments in the backscattering configuration used here dictate that the monopole transitions with $\Delta M = 0$ are the inter-shell modes active in light scattering experiments [20, 21, 22]. The lowest-energy transitions seen in Fig. 5.2 are thus interpreted as monopole transitions. In the FD framework such transitions are linked to $\Delta N = 2$.

5.2 The discovery of a new excitation

Since the QDs are in the few electron regime, it can thus be expected a large sensitivity of the excitation spectra on the incident laser intensity due to the impact of photo-generated electrons (actually of electron-hole pairs).

Figure 5.3 shows the evolution of spin and charge excitations from QDs with diameter D = 210 nm (shown in Fig. 5.1) as a function of the incident laser intensity in the range from 8.3 to 0.08 mW/cm^3. The laser photon energy was set at 1567 meV at the best resonance for both channels. The evolution of the signal from this sample displays a change in the shape of the spin spectra as the power is reduced. In fact the spectrum at the lowest intensity manifests a new excitation. The observation of this new spin mode indicates a clear change in the ground state that, as it will be argued in the next section, represents the fingerprint of a specific spin and charge configuration and reveals that the QDs are populated by four electrons.

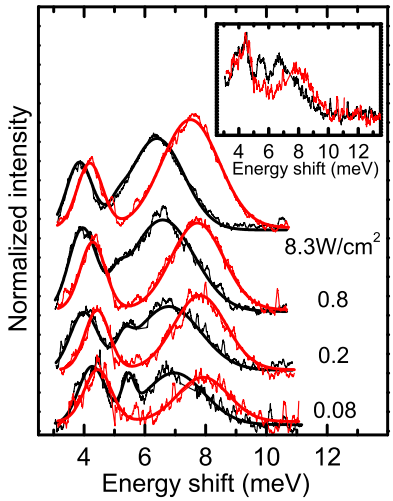

FIGURE 5.3: Evolution of charge (red) and spin (black) excitations as a function of the incident laser intensity. The resonant laser energy is 1567 meV. The inset displays a representative example of the spectra at 0.08 W/cm^2 before background subtraction.

5.3 Quantum dots with four electrons

The lowest intensity spectrum (I=0.08W/cm^2) in Fig. 5.3 reveals a sharp excitation in the spin channel at 5.5 meV. To interpret the origin of this sharp spin mode, it can be noted that if the ground state is a triplet with S = 1, a triplet-to-singlet (TS) inter-shell spin mode with ΔS = -1 can occur in addition to the lowest energy ΔS = +1 monopole excitation (see the representation of the excitations shown in Fig. 2.9). Such TS excitation is split from the ΔS = +1 mode, which is seen at lower energy by the difference in exchange and correlation contributions. On this basis the sharp peak at 5.5 meV is identified with the TS ($\Delta S = -1$) inter-shell spin excitation. According to Hund's rules a triplet ground state occurs only when two electrons are in a partially populated shell as in the case of QDs with four electrons. In the following, the experimental evidences of this interpretation will be presented together with comparison with theoretical calculations.

First it should be noted that a characteristic feature of the doublets observed close to 4 meV and 7 - 8 meV is their significant line-widths. This is attributed largely to inhomogeneous broadening due to small differences in effective confinements of the dots that may cause a distribution of the electron occupation of

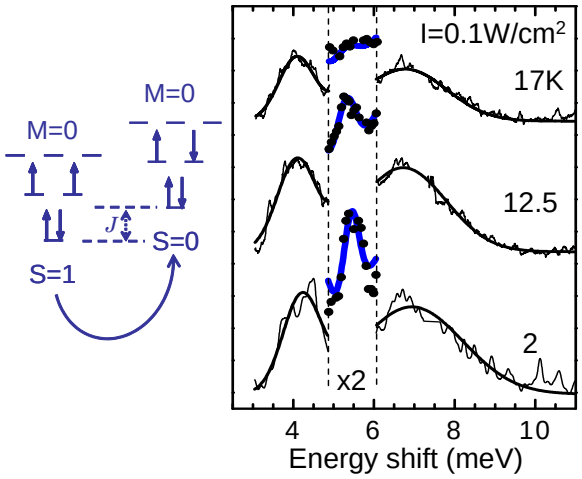

FIGURE 5.4: Temperature dependence of spin transitions. The laser intensity is I = 0.1 W/cm^2. Spectra are presented after conventional subtraction of background due to laser light. The cartoons in the left show a non-interacting representation of the S=1 ground state and of the lowest energy S=0 singlet state with M=0. The energy separation between these two states is the exchange energy J.

the QDs. In this framework the narrower width of the TS spin transition at 5.5 meV can be simply explained due to the absence of inhomogeneous broadening from the distribution of electron populations of the QDs since that excitation exists only in the case of the four-electron occupation.

Figure 5.4 shows the temperature dependence of spin transitions at a laser intensity I = 0.1 W/cm^2. It can be seen that contrary to the other inter-shell modes, the intensity of the TS spin excitation decreases significantly as the temperature increases with an estimated activation gap of 0.7 ± 0.3 meV. In fact this is also consistent with the assignment of the mode at 5.5 meV with the TS transition if one considers that at such low energy a possible thermally populated excited level is the S=0 singlet state without any change in orbital occupation. This energy provides an estimate of the low lying intra-shell singlet-triplet transition of the four-electron QDs and it compares well with CI estimate of 0.8 meV (energy difference between the triplet S = 1 and singlet S = 0 states with M =0, see the cartoon in Fig. 5.4).

The evolution of the spin transitions at different incident laser intensities shown in Fig. 5.3 is also consistent with the four electron interpretation. As the intensity increases additional electrons are expected to be photo-generated. The peaks display a red shift and the TS transition disappears at around I = 1 W/cm^2, suggesting that at this intensity all the QDs have more than 4 electrons and

therefore the number of those photo-generated is at least one. This is in clear contrast with the power dependence exhibited by the QDs with many electrons described in the previous chapter. In that case no significant changes in the QD spectra were detected as a function of the excitation power. This difference in the behavior of QDs with a diameter of 400 nm and 210 nm is not surprising since the change of one or two electrons is not expected to modify the properties of the QD with tens of electrons (which is the case of the QDs with D = 400 nm) but it is expected to deeply affect the properties of QDs in the few-electron regime.

5.4 Theoretical analysis of light scattering spectra

As shown above the prominent feature of the spectra of QDs with four electrons is the additional spin mode that emerges at low temperature and low excitation powers. It occurs as a very narrow peak with light scattering polarization selection rules of spin excitations and it is interpreted as a $\Delta S = -1$ inter-shell spin mode characteristic of a $S = 1$ triplet ground state with four electrons. The theoretical calculations presented in this section confirm this interpretations and suggest that the observed splitting between the low-lying spin modes with $\Delta S = 1$ and $\Delta S = -1$ represents a direct manifestation of the role of correlations in the excitation spectra of few-electron QDs.

In fact, numerical evaluations within a configuration-interaction (CI) theory [4, 33, 37] are able to reproduce the experimental light scattering spectra with a great precision that is not achieved by HF theory. The comparison of mean field and CI calculations uncovers large exchange and correlation terms of electron interactions that in the case of the four-electron triplet state are found to be comparable to quantum confinement energies.

The CI approach combined with calculations of the Raman cross-section [4, 33, 37, 34, 49, 75] was used for the numerical evaluation of the energy and intensity of low-lying spin and charge excitations of the interacting system with N_e electrons [1] (details can be found in appendix B).

Figure 5.5 compares excitation spectra at the lowest intensity with theoretical calculations of the Raman cross section of four electrons. As stated above the spin and charge excitations are detected with crossed (black) and parallel (red) polarization between incident and scattered light, respectively [76]. Pairs of peaks are seen at energies close to 4 meV and $7 - 8$ meV and interpreted as monopole excitations with $\Delta S = 1$ (spin) or $\Delta S = 0$ (charge). In the non-interacting FD picture these two excitations are degenerate but they split in the presence of exchange and depolarization contributions.

[1] Calculations were carried out by Massimo Rontani, Guido Goldoni and Elisa Molinari, CNR-INFM S3 Modena

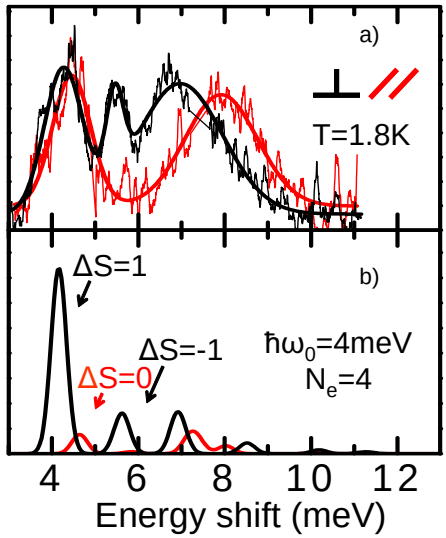

FIGURE 5.5: (a) Experimental low-temperature (T = 1.8 K) polarized (parallel incident and scattered photon polarizations, in red) and depolarized (perpendicular incident and scattered light polarizations, in black) resonant inelastic light scattering spectra after conventional subtraction of the background due to laser light and luminescence. Incident laser energy is 1567 meV, intensity is I = 0.08 W/cm^2 and integration time is 30 minutes. Fits of the data with three gaussians are shown. (b) Theoretical spectra for electron occupation $N_e = 4$ and $\hbar\omega_0 = 4$ meV. Gaussian line-shapes with a phenomenological standard deviation $\sigma = 0.18$ meV are used.

Figure 5.5(b) displays the calculated spectra for $N_e = 4$ and $\hbar\omega_0 = 4$ meV. The latter value was determined by fitting the peak energy position in the experimental spectra shown in Fig. 5.5(a). An independent check for these values of ω_0 and N_e comes from the empirical relation given by Eq. 3.3 linking N_e, ω_0, and the electron density, which yields $n_e = 1.2 \times 10^{11}$ cm^{-2}, in good agreement with the experimental value. Additionally the ground state for a QD with a confinement energy $\hbar\omega_0 = 4$ meV has a mean radius of ≈ 30 nm. This corresponds to a depletion width of ≈ 90 nm, in agreement with values obtained in section 3.1.3.

Figure 5.5(b) demonstrates that among all calculated excitations with $\Delta M = 0$, only a few of them turn out to have significant intensities, generating discrete spectrum lines (with a phenomenological broadening chosen to reproduce the measured TS linewidth) in very good agreement with the experimental ones. It can also be noted that more than one excitation gives a significant contribution to the spectra at energies above the TS mode. This is consistent with the observed larger linewidths for the higher-energy excitation pairs. Figure 5.6 reports the

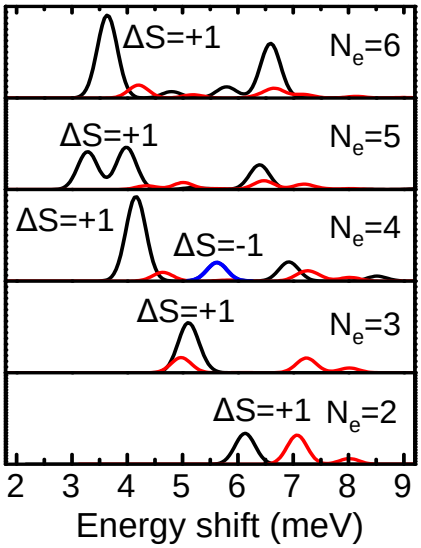

FIGURE 5.6: Evolution of the theoretical inelastic light scattering spectra as a function of electron occupation number N_e within a configuration-interaction approach. Red (black) curves represent charge (spin) excitations. The blue peak is the TS monopole inter-shell mode.

evolution of the calculated spectra as a function of N_e. As expected, the TS ($\Delta S = -1$) mode is peculiar to $N_e = 4$ and it is not observed at any other explored electron occupation configurations.

The excitations in Fig. 5.6 show a redshift of the lowest-energy features in both channels as N_e increases due to screening effect. Because of the exchange energy gain of excited states, the spin channel energy is systematically lower than the charge excitation energy. This large sensitivity of the light scattering spectra on particle occupation is at the origin of the difference between the observed linewidths of our inter-shell excitations. Comparing the evolution of peak energies shown in Fig. 5.6 with measured line-widths it can be concluded that a distribution of electron occupation between 4 and 6 characterizes our QD arrays. It also indicates that the light scattering method allows to probe excitation spectra of few-electron QDs with single-electron accuracy despite the relatively large number of QDs illuminated. As mentioned before, consistent with the assignment that links the $\Delta S = -1$ mode to those selected QDs that have four electrons, is the observed sharp linewidth of 0.4 meV which is much lower than the linewidths of the other spin and charge transitions.

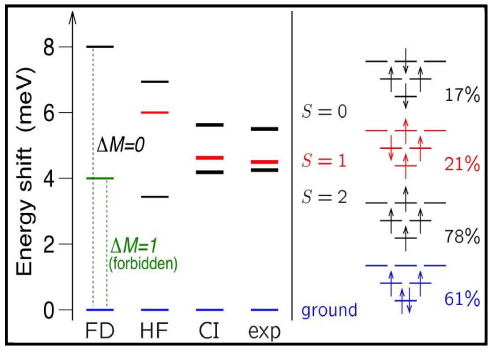

FIGURE 5.7: Comparison between measured (*exp* column) and calculated energies of charge (red) and spin (black) excitations, identified by arrows in Fig. 5.5 b): From left to right, non-interacting Fock-Darwin model (FD), self-consistent Hartree-Fock (HF), full configuration interaction (CI). Side diagrams show the most-weighted configurations in the CI linear expansion of the correlated wave functions, with the corresponding weight percentage. HF calculations refer to such configurations.

5.5 Evaluation of correlation effects

A specific feature of the theoretical evolutions in the low-N_e regime studied here is that states are represented by superpositions of many different SDs to incorporate both radial and angular spatial correlation [77, 63]. The side diagrams of Fig. 5.7 represent the predominant SDs in the CI expansion of the $N_e = 4$ ground and excited states involved in the three transitions indicated by arrows in Fig. 5.5(b). The weight percentage in the expansion of the exact states are also included. The states corresponding to the maximum allowed S_z are depicted, while in the actual calculation only the degenerate states with $S_z = 0$ were considered.

Figure 5.7 also shows ground- and excited-state energies calculated with different approximations that provide evidence for correlation effects in the excitation spectra. In the FD picture the energy difference between consecutive levels is given by $\hbar\omega_0 = 4$ meV. In the HF approach, the orbital states are computed self-consistently [78]. The energy difference between the three spin configurations is given by bookkeeping the exchange energy J gained each time two electron spins, occupying any orbitals a and b, are parallel to each other. This gain is accounted for by the Coulomb exchange integral between orbitals a and b described by FD wave functions. This approach neglects spatial correlation among electrons.

Correlation effects are included in the CI approach, leading to the theoretical spectra in Figs. 5.5 and 5.6 and to the quantitative agreement with experiments

shown in Fig. 5.7. The comparison between HF and CI (Fig. 5.7) suggests that correlation affects the relative splittings between excited states, even reversing their relative amplitudes: The $S = 1$ state is closer to $S = 0$ than to $S = 2$ in HF, while the opposite occurs in CI, in agreement with the experiment. As suggested by the decreasing contribution of the most weighted SD configurations indicated on the right in Fig. 5.7, correlation effects are small for the ground and the $S = 2$ excited state, but become increasingly important for excited states with smaller S. As S decreases, in fact, exchange interaction is less effective in keeping electrons far apart and excited states become more correlated. It should be noted that the relative amplitudes of the calculated HF and CI gaps are quite insensitive to the specific value of $\hbar\omega_0$ and that the measured splittings among the spin modes can only be reproduced by CI calculations, no matter the value of $\hbar\omega_0$.

In conclusion, these experiments provided direct measurements of the energies of spin and charge excitations in nano-fabricated quantum dots with four electrons. The characteristic excitations of the triplet configuration with four electrons have been identified and theoretically evaluated. These experiments show that inelastic light scattering methods offer a wealth of information on the physics of spin states in QDs with few electrons.

5.6 Ground state transitions induced by the magnetic field

The electronic structure of quantum dots under a magnetic field perpendicular to the in-plane direction displays a rich scenario of different phases of the ground state. An overwhelming amount of literature on this topic has been published. In particular a ground state transition at low magnetic fields was observed in QDs with four electrons by magneto-transport methods (see Fig. 2.3). The evolution of the CB peaks was linked to a ground-state transition between the triplet S=1 state at B=0 to a singlet S=0 state. In a mean-field framework, this transition is caused by the interplay between the exchange energy and the orbital cyclotron frequency. In fact when the cyclotron energy $\hbar\omega_c$ becomes equal to the splitting J between the triplet and singlet configurations a transition between these two ground states occurs.

The effect of a magnetic field on the triplet ground state with four electrons is also seen in the inelastic light scattering spectra. It will be shown below that the QD excitations undergo significant changes which can be observed in both the spin and charge channels.

The magnetic field experiments were carried out in the dilution cryostat with optical access and at temperatures T $\approx$ 200 mK (see the description of the optical set-up in section 3.2.3). 100×100μm arrays of QDs similar to the ones described

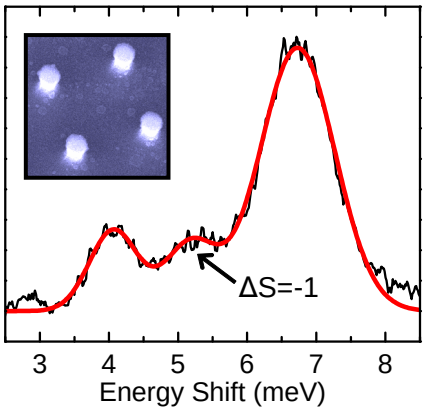

FIGURE 5.8: Inelastic light scattering spectrum in depolarized configuration from QDs with four electrons. The spectrum is shown after background subtraction and a fit with three gaussian functions has been included. Experiments were performed in a dilution cryostat at a temperature of T = 200 mK. The center peak close to 5meV is attributed to the triplet to singlet inter-shell excitation. Inset shows a SEM image of the QDs with a geometrical diameter of D ≈ 200 nm.

previously were fabricated for the studies presented in this section. The estimated metallurgical diameter of these dots (see inset to Fig. 5.8) was D ≈ 200 nm. At zero magnetic field the spectra from the QD array exhibited the typical charge and spin excitations of QDs with four electrons as described in the previous section. Figure 5.8 shows a representative inelastic light scattering spectrum in the depolarized configuration that manifests the TS inter-shell excitation with $\Delta S = -1$ (peak at $\sim$ 5 meV) peculiar to the four electron configuration. Contrary to the spectra reported in Fig. 5.3 the linewidths of the spin modes seen in Fig 5.8 are all relatively sharp, close or less than $\sim$ 1 meV. This suggests that a better homogeneity in terms of electron occupation was achieved in this QD array.

Figure 5.9 (a) shows the magnetic field evolution of the spin excitations. Data are presented after conventional subtraction of the background and a fit with three gaussian functions is included for better identification of the excitations. Two phenomena are observed: 1) the intensity of the center peak (gray region in Fig. 5.9 (a)) increases with the applied magnetic field (see the inset to Fig. 5.9 (a)) and 2) the linewidth of this peak changes with magnetic field and it displays a maximum close to B = 0.3 T. At these values of the magnetic field the cyclotron energy ($\approx 0.5 \pm 0.2$ meV) becomes approximately equal to the calculated energy difference between the triplet ground state at at zero magnetic field (S = 0, M = 0) and the singlet state (S=0) with $M = 2$ ($\Delta E = 0.46$ meV). At this point a ground state transition occurs (see level diagrams in Fig 5.9 (a)).

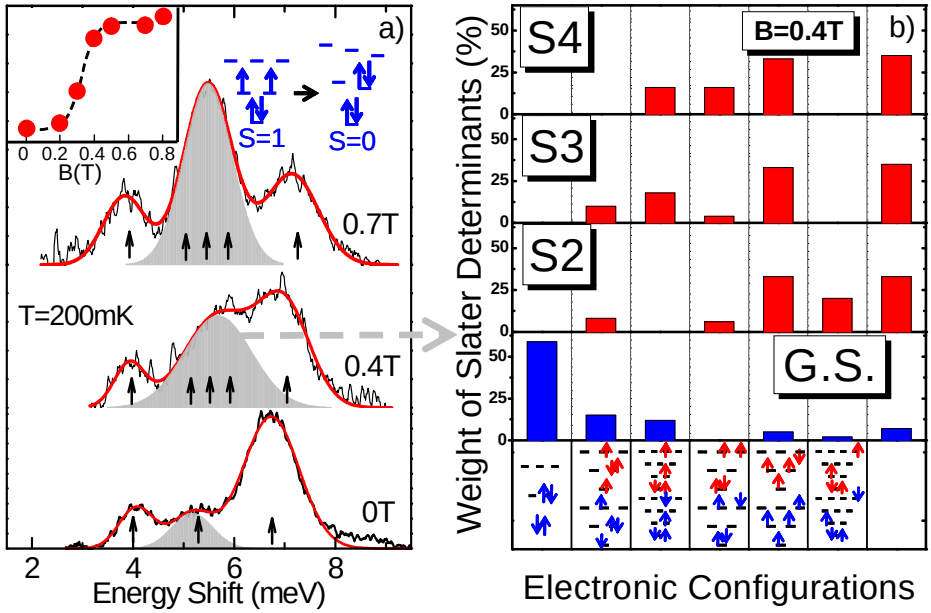

FIGURE 5.9: (a) Magnetic field evolution of the depolarized inelastic light scattering spectra in the range of $0 < B < 0.7$T. Data are presented after conventional subtraction of the background. A fit with three gaussian functions is also reported. The inset reports the evolution of the integrated intensities of the center peak as a function of the magnetic field B. (b) The histogram on the right shows the states that take part in the excitations that contribute to the center peak of the spectrum at magnetic field B=0.4T. A representation of the most-weighted Slater-Determinants that contribute to the wave-functions that take part in the excitations is shown at the bottom of the histogram. The columns above represent the weight percentage of these Slater determinants in the linear expansion of the exact states.

At zero magnetic field the S=1 ground state has total angular momentum M=0 and supports the monopole TS excitation as described in the previous section. The S=0 ground state at B = 0.4 T has a total angular momentum M = 2. CI calculations of the scattering cross section indicate that the TS mode is replaced by three closely-spaced spin excitations in the singlet state. The arrows below the spectra of Fig. 5.9(a) represent the energy of the calculated transitions with $\hbar\omega_0 = 3.75$ meV. The increase of the number of modes under the center peak after the ground state transition is consistent with the increase of the linewidth and intensity. This analysis thus offers direct evidence for the occurrence of a spin transition in the four-electron QDs at moderate values of the magnetic field.

The histograms shown in Fig. 5.9(b) summarize the SD configurations of the

states in the linear expansion of the exact states that contribute to the center peak of the spectrum at B = 0.4 T. SDs are represented at the bottom and the height of the columns provides the percentage of these SDs taking part to the excitation. This analysis highlights the role of correlations in the formation of the ground and excited states involved in the triplet-to-singlet ground-state transition probed by inelastic light scattering.

In conclusion, these experiments reveal the role of correlation in the spin transitions in quantum dots with few electrons. Since the usage of relatively small magnetic fields can modify the ground state angular momentum of the four-electron state, comparison of collective excitations between states with different M can be used in the low-density limit to study the formation of molecular-like roto-vibrational bands of a Wigner state.

Conclusions and perspectives

This thesis reported an experimental investigation of interaction phenomena of strongly correlated electrons confined in semiconductor QDs by means of measurements of collective excitations by inelastic light scattering. The observation of neutral spin and charge excitations in the regime of few-electron occupation in QDs represents the main achievement of this thesis work.

Instrumental to this study has been the optimization of the fabrication processes of homogeneous arrays of doped AlGaAs/GaA QDs by means of e-beam lithography and dry etching. Arrays of high quality QDs with in-plane parabolic confinement and different electron population have been realized. The high homogeneity and the the impact of the lateral confinement potential was probed by μ-PL experiments.

QDs with many electrons exhibit a shell structure revealed by a sequence of inter-shell excitations at energies that are multiplets of the confinement energy. In coupled QDs in the many-electron regime, the shell structure is modified by the interplay between the confinement energy and the tunneling gap giving

rise to several new peaks in the excitation spectra detected by inelastic light scattering. The results that have been presented here suggest that probing these excitations in coupled QDs with light scattering methods can provide a wealth of quantitative information on the energy level sequence, level occupation and tunneling gap in double QDs.

Spin and charge excitations from nano-fabricated AlGaAs/GaAs QDs with few electrons reveal a remarkably different behavior that allows to define a new regime where correlations play a central role in the interpretation of the spectra. The work presented in the last part of this thesis has focused on the study of QDs with four electrons. At zero magnetic field the four electrons are in a triplet spin state (S=1) and display a narrow spin excitation peak that has been assigned to the intershell triplet-to-singlet monopole mode. This excitation is a characteristic manifestation of the triplet state with four electrons. The QD system with four electrons also displays a rich phase diagram that can be explored by applying magnetic fields perpendicular to the QD plane. At small magnetic fields the system undergoes a transition from the triplet ground state with zero total angular momentum ($M = 0$) and total spin one ($S = 1$) to a state with total angular momentum two ($M = 2$) and zero total spin ($S = 0$). The light scattering experiments presented here has offered direct evidence for the occurrence of this spin transition. Large correlation effects that are comparable to exchange Coulomb interactions have been determined by comparing the experimental spectra with theoretical evaluations based on a configuration-interaction model.

The results presented in this work reveal the impact of correlation in the charge and spin configurations of QDs with few electrons. These studies are similar to those carried out in the field of fermionic particles confined in atomic nuclei [16]. In the early experiments on these systems, the collective nature of their excitations in the MeV spectral range was investigated by inelastic scattering of electrons and nucleons. Here the excitations are in the meV range and, remarkably, can be probed with application of light scattering methods even in the few-particle regime. In addition to their relevance for the understanding of the fundamental nature of electron interactions at the nanoscale, such correlated states of electrons in QDs are at the basis of quantum computation schemes [9, 10]. To this regard, the study of the excitation spectra of coupled QDs with two electrons represents a challenge for the continuation of this research activity.

By reducing the electron density and the confining potential of the QDs with few electrons the larger impact of correlation effects should eventually drive the electronic system into the fully localized regime of the Wigner molecular state [5, 3]. This regime is predicted to occur at densities remarkably larger than for crystallization in higher dimensions. From the perspectives of inelastic light scattering, this regime is particularly attractive since the excitation spectra

should be characterized by roto-vibrational bands. Indeed, while the threshold for Wigner localization due to correlation is hotly debated, evaluations indicate that insight into the impact of correlation could be gained by measurement of collective excitations. Access to states with different angular momenta, as obtained with applications of moderate magnetic fields in QDs with four electrons, could open the way to directly probe such roto-vibrational states by light scattering methods. Such observation of Wigner crystallization in QDs could be regarded as a significant milestone of the research activity in modern condensed-matter science.

Acknowledgments

I would like to thank a group of people that has made possible this thesis through their support to my work at the Scuola Normale Superiore and Lucent Technologies. I hope that life and science will bring us together to face new challenges:

I want to thank Vittorio Pellegrini, for the infinite patience that he employed with me during my learning process and writing of this thesis. I am thankful for his enormous contribution to my life and science education and for the trust in myself during many important moments. I would like to highlight here his great intuition to point out the relevant facts in our experiments. For all of these I consider myself very fortunate to have had a so talented advisor.

During these years I had the privilege to work under the supervision of Aron Pinczuk and Fabio Beltram. I would like to thank them for the continuous support, explanations and advices. It is an honor to be guided by them, and I hope to have deserved all the confidence that they deposited on me.

I thank also our co-workers from Modena University: Massimo Rontani, Guido Goldoni and Elisa Molinari, not only for the numerical calculations of QD states that appear in this thesis, but also for all the discussions and their great contribution to the understanding of the physics that we have discovered together. Working with them has been a pleasure and a privilege.

I would like to thank Sokratis Kalliakos, for all the science that we have shared and for understanding my moods and my way to act in the laboratory and to Brian Dennis that was a perfect teacher-partner during the time I spent in Bell-Labs.

I would like to mention that this work has been possible thanks to the crucial contribution of Loren Pfeiffer, Ken West, Lucia Sorba and Giorgio Biasiol that

provided state of the art MBE-grown samples for the fabrication of the QDs presented in this thesis.

I want to give a special acknowledge to Rüdeger Köhler for his support during my first years of my PhD and for teaching me how to face big challenges. He also made me believe more in myself. And for being a friend.

I am also grateful to Stefano Luin, Pasqualantonio Pingue, Vincenzo Piazza, Marco Cecchini and Stefano Roddaro, for sharing their knowledge with me, for their help in the laboratory and for their friendship.

I am conscious that this list of people and reasons should be longer. I apologize to all them whom I could not make appear here.

I would also like to thank my cousin Vicente García García for the drawings that have given the special touch of art to the thesis. I am a big fan of him.

I want to mention Virginia García that has been with me during this thesis.

Last but not least, I want to thank my family, it is a very big one (aunts, uncles and cousins that always care about me). All of them would deserve to be here because of their caring and support while I am far from home. Unfortunately I only have space to explicitly mention my parents Iñigo Pascual Parra and Josefina García García and my brother Raúl Pascual García, who in the moments of weakness were always there to give the correct advice. They have been always my best supporters and I am very proud of them.

Appendix

A Fabrication methods

A.1 Lithography

A LEO-1530 SEM was used for the lithography process. Samples were prepared following these steps:

- cleaning and drying on the hot-plate;
- spinning of e-beam resist **AR-P 679.02** at 6000 rpm for 60s
- baking 120^{o}C for 15min;
- exposure 30kV at working distance of about 10mm
- development **AR 600-56** for 2 min;
- stop in IPA

A.2 Thermal evaporation

Thermal evaporation was used to create the hard mask before the etching process. Ni masks of thickness of 20 to 30 nm were prepared using a standard thermal evaporator.

Pressure [Pa]	ICP Pwr [W]	Bias [V]	Time [sec]	BCl3 [sccm]	Cl_2 [sccm]	Ar [sccm]	Depth [nm]
0.1	400	70	120	4	10	3	510

TABLE A.1: Details of the etching process for samples in Figs. 4.1 and 5.1

A.3 Lift-off Protocol

After evaporation the sample is put in acetone for 10-20 minutes. The lift-off procedure can be started when the metallic layer starts to appear rough, due to the melting of the underlying resist (this could not happen for very thick evaporations). At this point the metal can be removed by spraying acetone with a syringe. If necessary a sonicator can be used to remove the remaining parts of the evaporated metal.

A.4 Dry etching by ICP-RIE

The Sentech SI 500 ICP etcher was used for AlGaAs/GaAs etching with Cl2/BCl3/Ar plasma chemistry. The samples were cleaned with acetone and then thermally contacted to a 4 silicon wafer which was used as a carrier.

The etching was carried out under the following conditions:

- plasma source: ICP, PTSA 200
- gases: Cl2, BCl3, Ar
- electrode temperature: 30C, He-backside cooling

The detailed processing conditions of the dry etching depended on the environment conditions that affected the reactor. These conditions were found to drift slowly with time. The details of the etching for the 400 nm and 210 nm QDs (Figs. 4.1 and 5.1) are provided in table A.1

Appendix

B

Description of the numerical calculations

The correlated wave-functions of ground and excited states were written as superpositions of SDs:

$$\left|\Phi_{\{\alpha_i\}}\right\rangle = \prod_{i=1}^{N_e} e^{\dagger}_{\alpha_i} |0\rangle \quad , \tag{B.1}$$

obtained by filling in the single-particle spin-orbitals α with the N electrons in *all* possible ways [$e^{\dagger}_{\alpha}$ creates an electron in level $\alpha \equiv (n, m, \uparrow \text{ or } \downarrow)$]. The resulting Hamiltonian was first block diagonalized, fully exploiting symmetries [34]. Finally, the Hamiltonian was diagonalized via Lanczos [79] method in each (M, S, S_z) sector, giving the low-energy excited states. The resonant Raman transition matrix elements A_{FI} between the fully interacting ground and excited states $|\mathrm{I}\rangle$ and $|\mathrm{F}\rangle$, respectively, were obtained, after the CI calculation, from:

$$A_{\mathrm{FI}} = \sum_{\alpha\alpha'} \gamma_{\alpha\alpha'} \left\langle \mathrm{F}|e^{\dagger}_{\alpha} e_{\alpha'}|\mathrm{I}\right\rangle \quad , \tag{B.2}$$

where $\gamma_{\alpha\alpha'}$ is the two-photon process matrix element between α and α' spin-orbitals, as defined in Ref. [35] within second order perturbation theory in the radiation field and containing resonant denominators.

$\gamma_{\alpha\alpha'}$ causes the enhancement of the light scattering intensity when the laser energy resonates with the optical gap. Coulomb interaction between electrons and heavy holes were neglected and a finite-width quantum well for both electrons and holes was considered. Spectra were computed under resonance con-

ditions, with laser energy larger than optical gap, and $q = 1 \times 10^4$ cm^{-1}. The calculated intensities were found to depend to the chosen laser energy.

Bibliography

[1] S. M. Reimann and M. Manninen, *Rev. Mod. Phys.* **74**, 1283 (2002).

[2] G. W. Bryant, *Phys. Rev. Lett.* **59**, 1140 (1987).

[3] A. Ghosal, A. D. Güçlü, C. J. Umrigar, D. Ullmo, and H. U. Baranger, *Nature Physics* **2**, 336 (2006).

[4] M. Rontani, G. Goldoni, F. Manghi, and E. Molinari, *Europhys. Lett.* **58**, 555 (2002).

[5] R. Egger, W. Husler, C. H. Mak, and H. Grabert, *Phys. Rev. Lett.* **82**, 3320 (1999).

[6] O. Steffens and M. Suhrke, *Phys. Rev. Lett.* **82**, 3894 (1999).

[7] C. H. Bennett, *Physics today* **48**, 24 (1995).

[8] J. I. Cirac and P. Zoller, *Phys. Rev. Lett.* **74**, 4091 (1995).

[9] D. Loss and D. P. DiVincenzo, *Phys. Rev. A* **57**, 120 (1998).

[10] D. P. DiVincenzo, D. Bacon, J. Kempe, G. Burkard, and K. B. Whaley, *Nature* **408**, 339 (2000).

[11] G. Burkard, D. Loss, and D. P. DiVincenzo, *Phys. Rev. B* **59**, 2070 (1999).

[12] A. Imamoglu, D. D. Awshalom, G. Burkard, D. P. DiVincenzo, D. Loss, M. Sherwin, and A. Small, *Phys. Rev. Lett.* **83**, 4204 (1999).

[13] L. P. Kouwenhoven, C. M. Marcus, P. L. Mceuen, S. Tarucha, R. M. Westervelt, and N. S. Wingreen, *Proceedings of the Advanced Study Institute on Mesoscopic Electron Transport*, 1997.

[14] S. Tarucha, D. G. Austing, Y. Tokura, W. G. van der Wiel, and L. P. Kouwenhoven, *Phys. Rev. Lett.* **84**, 2485 (2000).

[15] L. P. Kouwenhoven, D. G. Austing, and S. Tarucha, *Rep. Prog. Phys.* **64**, 701 (2001).

[16] B. R. Mottelson, *Nobel lecture, December 11, 1975*, Nobel, Nordita, Copenhagen Denamark, 1975.

[17] G. Abstreiter, M. Cardona, and A. Pinczuk, in *Light scattering in solids IV*, edited by M.Cardona and G. Guntherodt, page 5, Springer-Verlag, Berlin Heidelberg NewYork Tokyo, 1984.

[18] A. Pinczuk, S. Schmitt-Rink, G. Danan, J. P. Valladares, L. N. Pfeiffer, and K. W. West, *Phys. Rev. Lett.* **63**, 1633 (1989).

[19] M. Cardona, editor, *Light Scattering in Solids I*, Springer-Verlag, Berlin Heidelberg, 1983.

[20] D. J. Lockwood, P. Hawrylak, P. D. Wang, C. M. Sotomayor Torres, A. Pinczuk, and B. S. Dennis, *Phys. Rev. Lett.* **77**, 354 (1996).

[21] R. Strenz, U. Bockelmann, F. Hirler, G. Abstreiter, G. Böhm, and G. Weimann, *Phys. Rev. Lett.* **73**, 3022 (1994).

[22] C. Schüller, K. Keller, G. Biese, E. Ulrichs, L. Rolf, C. Steinebach, D. Heitmann, and K. Eberl, *Phys. Rev. Lett.* **80**, 2673 (1998).

[23] P. C. Sercel and K. J. Vahala, *Phys. Rev. B* **42**, 3690 (1990).

[24] A. Delgado, A. Gonzalez, and D.J. Lockwood, *Phys. Rev. B* **69**, 155314 (2004).

[25] D. Heitmann and J. P. Kotthaus, *Physics today* **June**, 56 (1993).

[26] Ch. Sikorski and U. Merkt, *Surf. Sci.* **229**, 282 (1990).

[27] Ch. Sikorski and U. Merkt, *Phys. Rev. Lett.* **62**, 2164 (1989).

[28] M. Korkusiski, P. Hawrylak, M. Ciorga, M. Pioro-Ladrire, and A. S. Sachrajda, *Phys. Rev. Lett.* **93**, 206806 (2004).

[29] S. Tarucha, D.G. Austin, T. Honda, R.J. van der Haage, and L. Kouwenhoven, *Phys. Rev. Lett.* **77**, 3613 (1996).

[30] L. P. Kouwenhoven, T. H. Oosterkamp, M. W. S. Danoesastro, M. Eto, D. G. Austing, T. Honda, and S. Tarucha, *Science* **278**, 1788 (1997).

[31] M. Fujito, A. Natori, and H. Yasunaga, *Phys. Rev. B* **53**, 9952 (1996).

[32] Y. Tanaka and H. Akera, *Phys. Rev. B* **53**, 3901 (1996).

[33] M. Rontani, S. Amaha, K. Muraki, F. Manghi, E. Molinari, S. Tarucha, and D. G. Austing, *Phys. Rev. B* **69**, 085327 (2004).

[34] M. Rontani, C. Cavazzoni, D. Bellucci, and G. Goldoni, *J. of Chem. Phys.* **124**, 124102 (2006).

[35] C. Steinebach, C. Schüller, and D. Heitmann, *Phys. Rev. B* **59**, 10240 (1999).

[36] D. Pfannkuche, V. Gudmundsson, and P. A. Maksym, *Phys. Rev. B* **47**, 2244 (1993).

[37] D. Bellucci, M. Rontani, F. Troiani, G. Goldoni, and E. Molinari, *Phys. Rev. B* **69**, 201308 (2004).

[38] U. Meirav, M. A. Kastner, and S. J. Wind, *Phys. Rev. Lett.* **65**, 771 (1990).

[39] R. C. Ashoori, H. L. Stormer, J. S. Weiner, L. N. Pfeiffer, S. J. Pearton, K. W. Baldwin, and K. W. West, *Phys. Rev. Lett.* **68**, 3088 (1992).

[40] C. Ellenberger, T. Ihn, C. Yannouleas, U. Landman, K. Ensslin, D. Driscoll, and A. C. Gossard, *Phys. Rev. Lett.* **96**, 126806 (2006).

[41] F. R. Waugh, M. J. Berry, D. J. Mar, R. M. Westervelt, K. L. Campman, and A. C. Gossard, *Phys. Rev. Lett.* **75**, 705 (1995).

[42] D. Dixon, L. P. Kouwenhoven, P. L. McEuen, Y. Nagamune, J. Motohisa, and H. Sakaki, *Phys. Rev. B* **53**, 12625 (1996).

[43] J. R. Petta, A. C. Johnson, J. M. Taylor, E. A. Laird, A. Yacoby, M. D. Lukin, C. M. Marcus, M. P. Hanson, and A. C. Gossard, *Science* **309**, 2180 (2005).

[44] F. M. Peeters, *Phys. Rev. B* **42**, 1486 (1990).

[45] L. Brey, N. F. Johnson, and B. I. Halperin, *Phys. Rev. B* **40**, 10647 (1989).

[46] W. Kohn, *Phys. Rev.* **123**, 1242 (1961).

[47] T. Brocke, M. T. Bootsmann, M. Tews, B. Wunsch, D. Pfannkuche, Ch. Heyn, W. Hansen, D. Heitmann, and C. Schüller, *Phys. Rev. Lett.* **91**, 257401 (2003).

[48] A. Delgado, A. Gonzalez, and E. Menndez-Proupin, *Phys. Rev. B* **65**, 155306 (2002).

[49] P. Hawrylak, *Solid State Commun.* **93**, 915 (1995).

[50] Ll. Serra, M. Barranco, A. Emperador, M. Pi, and E. Lipparini, *Phys. Rev. B* **59**, 15290 (1999).

[51] A. Mooradian, *Phys. Rev. Lett.* **20**, 1102 (1968).

[52] R. Decca, A. Pinczuk, S. Das Sarma, S. Dennis, L. N. Pfeiffer, and K. W. West, *Phys. Rev. Lett.* **72**, 1506 (1994).

[53] C. Pascual Garcia, V. Pellegrini, A. Pinczuk, M. Rontani, G. Goldoni, E. Molinari, B. S. Dennis, L. N. Pfeiffer, and K. W. West, *Phys. Rev. Lett.* **95**, 266806 (2005).

[54] S. Agarwala, S. C. Horst, O. King, K. Wilson, D. Stone, M. Dagenais, and Y. J. Chen, *J.Vac.Sci.Technol.B* **16**, 511 (1998).

[55] M. Sugawara, *Plasma Etching*, Oxford Science Publications, Oxford University Press, 1998.

[56] G. Grosso and G. Pastori Paravicini, *Solid State Physics*, Elsevier, 2000.

[57] J. Martorell and D. W. L. Sprung, *Phys. Rev. B* **54**, 11386 (1996).

[58] J. Kirschbaum, E. M. Höhberger, R. H. Blick, W. Wegscheider, and M. Bichler, *Appl. Phys. Lett.* **81**, 280 (2002).

[59] K. K. Choi, D. C. Tsui, and K. Alavi, *Appl. Phys. Lett.* **50**, 110 (1987).

[60] R. Sasagawa, H. Sugawara, Y. Ohnoand H. Nakajima, S. Tsujino, H. Akiyama, and H. Sakaki, *Appl. Phys. Lett.* **72**, 719 (1998).

[61] S. Kalliakos, C. Pascual Garcia, V. Pellegrini, M. Zamfirescu, L. Cavigli, M. Gurioli, A. Vinattieri, A. Pinczuk, B. S. Dennis, L. Pfeiffer, and K. W. West, *Appl. Phys. Lett.* **90**, 181902 (2007).

[62] R. J. Warburton, C. Shäflein, D. Haft, F. Bickel, A. Lorke, K. Karrai, J.M. Garcia, W. Shoenfeld, and P. M. Petroff, *Nature* **405**, 926 (2000).

[63] C. Schüller, C. Steinebach, and D. Heitmann, *Solid State Commun.* **119**, 323 (2001).

[64] T. Hatano, M. Stopa, and S. Tarucha, *Science* **309**, 268 (2005).

[65] T. H. Wang and S. Tarucha, *Appl. Phys. Lett.* **71**, 2499 (1997).

[66] H. J. Krenner, M. Sabathil, E. C. Clark, A. Kress, D. Schuh, M. Bichler, G. Abstreiter, and J. J. Finley, *Phys. Rev. Lett.* **94**, 057402 (2005).

[67] C. Pascual García, S. Kalliakos, V. Pellegrini, A. Pinczuk, B. S. Dennis, L. N. Pfeiffer, and K. W. West, *Appl. Phys. Lett.* **88**, 113105 (2006).

[68] J. M. Elzerman, R. Hanson, L. H. Willems van Beveren, B. Witkamp, L. M. K. Vandersypen, and L. P. Kouwenhoven, *Nature* **430**, 431 (2004).

[69] T. Fujisawa, D. G. Austing, Y. Tokura, Y. Hirayama, and S. Tarucha, *Nature* **419**, 278 (2002).

[70] A. Kogan, G. Granger, M. A. Kastner, D. Goldhaber-Gordon, and Hadas Shtrikman, *Phys. Rev. B* **67**, 113309 (2003).

[71] J. R. Petta, A. C. Johnson, A. Yacoby, C. M. Marcus, M. P. Hanson, and A. C. Gossard, *Phys. Rev. B* **72**, 161301 (2005).

[72] D. M. Zumbhl, C. M. Marcus, M. P. Hanson, and A. C. Gossard, *Phys. Rev. Lett.* **93**, 256801 (2004).

[73] M. Bayer, T. Gutbrod, A. Forchel, V. D. Kulakovskii, A. Gorbunov, M. Michel, R. Steffen, and K. H. Wang, *Phys. Rev. B* **58**, 4740 (1998).

[74] M. Kroutvar, Y. Ducommun, D. Heiss, M. Bichler, D. Schuh, G. Abstreiter, and J. J. Finley, *Nature* **432**, 81 (2004).

[75] A. Wójs and P. Hawrylak, *Phys. Rev. B* **56**, 13227 (1997).

[76] V. Pellegrini and A. Pinczuk, *Solid State Commun.* **119**, 301 (2001).

[77] C. Steinebach, C. Schüller, and D. Heitmann, *Phys. Rev. B* **61**, 15600 (2000).

[78] M. Rontani, F. Rossi, F. Manghi, and E. Molinari, *Phys. Rev. B* **59**, 10165 (1999).

[79] R. B. Lehoucq, K. Maschhoff, D. C. Sorensen, and C. Yang, "Lanczos ARPACK computer code", 1997, `http://www.caam.rice.edu/software/ARPACK/`.